Three-Dimensional Electrical Resistivity Tomography of the Solfatara Crater (Italy): Implication for the Multiphase Flow Structure of the Shallow Hydrothermal System

Marceau Gresse, Jean Vandemeulebrouck, Svetlana Byrdina, Giovanni Chiodini, André Revil, Timothy Johnson, Tullio Ricci, Giuseppe Vilardo, Annarita Mangiacapra, Thomas Lebourg, et al.

AGU PUBLICATIONS

JGR

Journal of Geophysical Research: Solid Earth

RESEARCH ARTICLE
10.1002/2017JB014389

Key Points:
- A 3-D gas-dominated reservoir feeds the Bocca Grande fumarole at 164 degrees Celsius through a ~10 m thick conduit
- The Fangaia mud pool and Pisciarelli fumarole are both conductive liquid-dominated plume
- A buried fault drives the condensate water from the main fumaroles toward the Fangaia mud pool

Supporting Information:
- Movie S1
- Movie S2
- Table S1
- Supporting Information S1

Correspondence to:
M. Gresse,
marceau.gresse@gmail.com

Citation:
Gresse, M., Vandemeulebrouck, J., Byrdina, S., Chiodini, G., Revil, A., Johnson, T. C., … Metral, L. (2017). Three-dimensional electrical resistivity tomography of the Solfatara crater (Italy): Implication for the multiphase flow structure of the shallow hydrothermal system. *Journal of Geophysical Research: Solid Earth*, *122*, 8749–8768. https://doi.org/10.1002/2017JB014389

Received 28 APR 2017
Accepted 6 OCT 2017
Accepted article online 10 OCT 2017
Published online 27 NOV 2017

Three-Dimensional Electrical Resistivity Tomography of the Solfatara Crater (Italy): Implication for the Multiphase Flow Structure of the Shallow Hydrothermal System

Marceau Gresse[1], Jean Vandemeulebrouck[1], Svetlana Byrdina[1], Giovanni Chiodini[2], André Revil[1], Timothy C. Johnson[3], Tullio Ricci[4], Giuseppe Vilardo[5], Annarita Mangiacapra[5], Thomas Lebourg[6], Jacques Grangeon[1], Pascale Bascou[1], and Laurent Metral[1]

[1]Univ. Grenoble Alpes, Univ. Savoie Mont Blanc, CNRS, IRD, IFSTTAR, ISTerre, Grenoble, France, [2]Istituto Nazionale di Geofisica e Vulcanologia, Bologna, Italy, [3]Pacific Northwest National Laboratory, Energy and Environment Directorate, Richland, WA, USA, [4]Istituto Nazionale di Geofisica e Vulcanologia, Rome, Italy, [5]Istituto Nazionale di Geofisica e Vulcanologia, Osservatorio Vesuviano, Naples, Italy, [6]Géosciences Azur UMR 6526, Nice, France

Abstract The Solfatara volcano is the main degassing area of the Campi Flegrei caldera, characterized by 60 years of unrest. Assessing such renewal activity is a challenging task because hydrothermal interactions with magmatic gases remain poorly understood. In this study, we decipher the complex structure of the shallow Solfatara hydrothermal system by performing the first 3-D, high-resolution, electrical resistivity tomography of the volcano. The 3-D resistivity model was obtained from the inversion of 43,432 resistance measurements performed on an area of ~0.68 km^2. The proposed interpretation of the multiphase hydrothermal structures is based on the resistivity model, a high-resolution infrared surface temperature image, and 1,136 soil CO_2 flux measurements. In addition, we realized 27 soil cation exchange capacity and pH measurements demonstrating a negligible contribution of surface conductivity to the shallow bulk electrical conductivity. Hence, we show that the resistivity changes are mainly controlled by fluid content and temperature. The high-resolution tomograms identify for the first time the structure of the gas-dominated reservoir at 60 m depth that feeds the Bocca Grande fumarole through a ~10 m thick channel. In addition, the resistivity model reveals a channel-like conductive structure where the liquid produced by steam condensation around the main fumaroles flows down to the Fangaia area within a buried fault. The model delineates the emplacement of the main geological structures: Mount Olibano, Solfatara cryptodome, and tephra deposits. It also reveals the anatomy of the hydrothermal system, especially two liquid-dominated plumes, the Fangaia mud pool and the Pisciarelli fumarole, respectively.

1. Introduction

Hydrothermal systems associated with active volcanoes involve fluids and heat transfer across porous and fractured rocks. Depending on temperature-pressure conditions, these systems can be either "liquid dominated" or "vapor dominated" (White et al., 1971). In the latter, near-surface gas condensation produces a large amount of water channeled into the ground and often released through acid streams (Hochstein & Sudarman, 1993).

For long-lived calderas, volcanic unrest is generally characterized by a pressurization of the hydrothermal system (e.g., Acoccella et al., 2015; Chiodini et al., 2016) leading to ground uplift and to changes in the composition and degassing rate of fumaroles (Caliro et al., 2014). Hydrothermal systems constitute therefore a critical element widely used to assess and monitor a renewal activity (e.g., Chiodini, 2009; Chiodini et al., 2002, 2012; Gottsmann et al., 2007; Tassi et al., 2013; Werner et al., 2012). Unraveling the shallow volcanic structure is of primary importance to properly assess the complexity of hydrothermal systems because knowledge of fluid pathway geometry can help to decipher a systematic hydrothermal response to magmatic activity.

Electrical resistivity tomography (ERT) and magnetotellurics (MT) are classical geophysical methods used to image shallow and deep hydrothermal systems thanks to the sensitivity of the electrical resistivity to the presence of thermal fluids and alteration (e.g., Aizawa et al., 2005; Byrdina et al., 2014; Finizola et al., 2004;

Hase et al., 2005; Revil et al., 2011, 2004). The electrical resistivity (or its inverse, the electrical conductivity) of rocks is influenced by two contributions, one associated with electrical conduction in the bulk pore fluid and one associated with the presence of an electrical double layer surrounding the grains. The first contribution depends on saturation, the ionic strength, and temperature of pore water (Revil et al., 2002; Roberts et al., 2001; Ussher et al., 2000). The second contribution, called surface conductivity, is mainly related to their cation exchange capacity (CEC) (e.g., Revil et al., 2017a, 2017b). High CEC values are generally associated with the formation of secondary minerals, such as clays, due to host rock alterations processes (Revil et al., 2017a, 2017b). Knowing which contribution between surface conductivity versus pore fluid conductivity dominates the observed conductivity response is a recurrent issue when interpreting electrical resistivity tomograms. Understanding resistivity images also requires soil temperature and CO_2 flux mappings in order to delineate the surficial extents of hydrothermal systems (e.g., Revil et al., 2008, 2011). In addition, self-potential measurements allow inference of the direction and the dynamics of hydrothermal circulations (e.g., Ishido, 2004; Revil et al., 2011; Villasante-Marcos et al., 2014) (Text S1 in the supporting information).

Most volcanic edifices are polygenetic structures, comporting inherited geological and tectonic features, which lead to complex spatial changes in both fluid circulations and geochemical processes. In the last decade, progress has been made to improve 3-D imaging and interpretation using ERT (Revil et al., 2010; Rosas-Carbajal et al., 2016). However, to date, studies have used low spatial resolutions (20 m or more between each measurement) to cover large areas and, therefore, cannot account for local effects and complex geometry.

In this study, we focus on the Solfatara volcano for the following reasons. Campi Flegrei caldera is presently experiencing unrest (Chiodini et al., 2016), characterized by an intense degassing, with ~2,000 t of CO_2 and some thousands of tons of H_2O released per day at the Solfatara (Chiodini et al., 2015), which can be compared to a small-scale volcanic eruption (Chiodini et al., 2012). The geochemical evolution of the fumaroles suggests an increase of temperature of the hydrothermal reservoir, while extension of the degassing area, ground uplift, and seismic swarms is still ongoing (Chiodini et al., 2016). This activity renewal needs to be better understood and assessed since approximately half million inhabitants live within the Campi Flegrei caldera. Moreover the Solfatara volcano is the most probable area of a future explosive eruption (Neri et al., 2015) that may be associated with very short precursor signals (Jolly et al., 2014). Finally, the small size of this crater with a diameter of ~700 m, extending on ~0.35 km^2 allows such high-resolution spatial imagery.

Here we present the first 3-D ERT model of the shallow hydrothermal system of the Solfatara volcano in the Campi Flegrei caldera (Italy). This 3-D model includes new high-resolution ERT data and thermal and soil CO_2 flux maps and uses self-potential and ERT data from Byrdina et al. (2014). The purpose of this work is to precisely recognize the main geological and hydrothermal structures, with a resolution up to 1 m, in order to understand the multiphase fluid circulation within the crater. We also aim to evaluate the contribution of grain surface conductivity with respect to fluid conductivity, in order to separate liquid-dominated structures from clay-rich areas.

2. Geological Settings

Extending over ~65 km^2, the volcanic region of the Campi Flegrei is located in the western metropolitan area of Naples (Italy). The Campi Flegrei is a long-lived nested caldera formed over the last 50 kyr by two major eruptions: the Campanian Ignimbrite and the Neapolitan Yellow Tuff, respectively, at ~39 kyr and ~12 kyr (see Figure 1a, and De Vivo et al., 2001). After the Neapolitan Yellow Tuff eruption, more than 70 mainly explosive eruptions occurred during three main epochs: 15.0–10.6, 9.6–9.1, and 5.5–3.8 kyr (Orsi et al., 2004; Smith et al., 2011; Vito et al., 1999). Monte Nuovo was the last historical eruption, which occurred in 1538 A.D. It was preceded by a ground uplift of several meters over few decades (Guidoboni & Ciuccarelli, 2011). The present activity started in the 1950s, with three main uplift episodes in the years 1950–1953, 1970–1972, and 1982–1984, each one accompanied by seismic swarms, with a cumulated ground uplift of ~3 m (Del Gaudio et al., 2010). This typical activity known as bradyseism has a double origin. The first one is related to the pressurization of a magmatic gas accumulation at 3–4 km depth

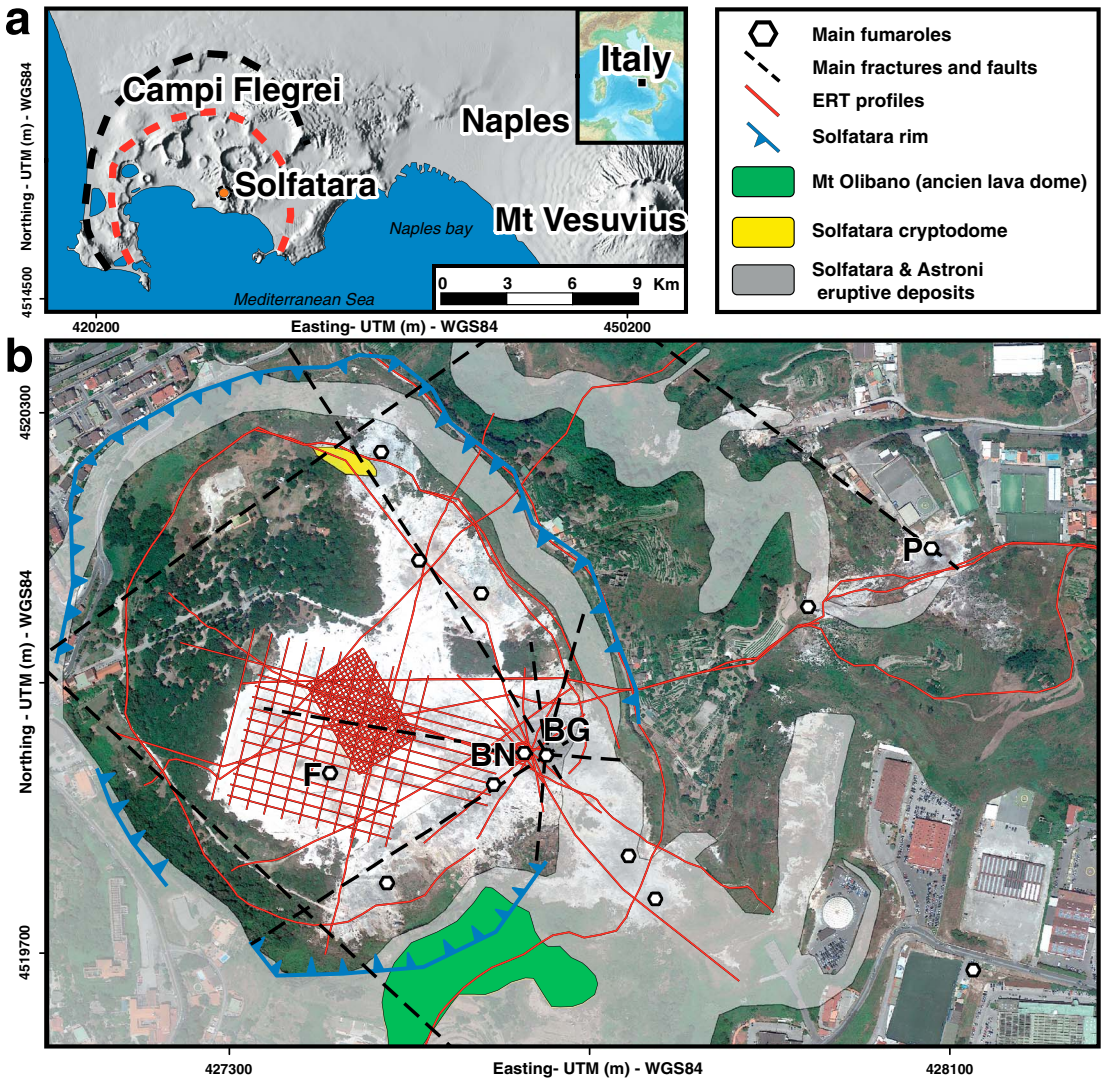

Figure 1. Map of the studied area and location of the ERT profiles. (a) The Solfatara crater inside the Campi Flegrei, in the Neapolitan urban area (GIS database from Bechtold et al., 2005). Two major eruptions formed nested calderas, Campanian Ignimbrite and Neapolitan Yellow Tuff calderas (black and red dotted line). (b) Solfatara satellite map (2014) with ERT profiles (red lines) crossing main geological units: Mount Olibano, Solfatara cryptodome, and eruptive deposits, after Isaia et al. (2015). Black dotted lines indicate the major fractures/faults, after D'Antonio et al. (1999) and Petrosino et al. (2012). Main vents are indicated with black circles: Bocca Grande (BG) and Bocca Nuova (BN) fumaroles and Fangaia mud pool (F) and the Pisciarelli fumarolic area (P).

(Chiodini et al., 2015). Its second origin is due to repeated CO_2-rich magmatic fluids injections from the magmatic gas reservoir into the hydrothermal system at 2 km depth inducing its pressurization and heating (Chiodini et al., 2016).

The Solfatara volcano, located at the center of the Campi Flegrei caldera, was formed 4.2 kyr ago by a series of phreatic and phreatomagmatic eruptions (Isaia et al., 2015). It was built over the Mount Olibano lava dome and several tephra deposits (Figure 1b) (Isaia et al., 2009, 2015). This volcano lies on the top of a hydrothermal plume driving a large amount of fluids toward the surface (Chiodini et al., 2001). These hot fluids—mainly H_2O and CO_2—exsolve from a magmatic body at a depth of 8 km then mix with meteoric components in a hydrothermal reservoir at 3–4 km depth (Zollo et al., 2008) (Figure 2). Finally, these fluids are released through diffuse and direct degassing at the surface of the Solfatara crater, a permeable maar-diatreme structure (Isaia et al., 2015), crossed by NW-SE and NE-SW ring faults (Chiodini et al., 2015; Dvorak & Gasparini, 1991; Rosi et al., 1983). The main surface hydrothermal features comprise the Fangaia mud pool, Bocca Grande and Bocca Nuova fumaroles, and a currently evolving fumarolic area at Pisciarelli (Figure 1b, 2, and 3).

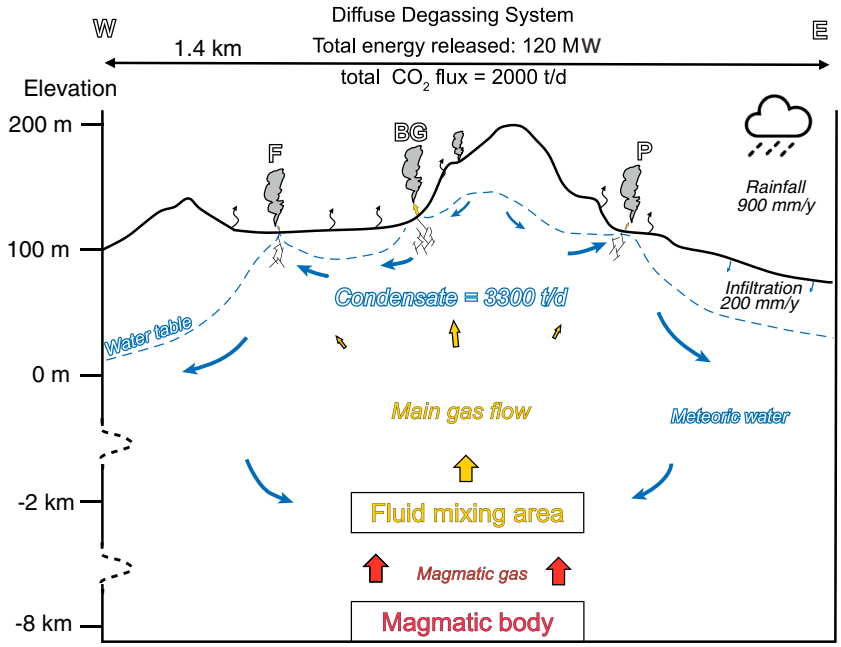

Figure 2. Conceptual model of the Solfatara hydrothermal system (modified after Bruno et al., 2007; Caliro et al., 2014; Chiodini et al., 2001; Ducci & Tranfaglia, 2005; Isaia et al., 2015; Petrosino et al., 2012; Zollo et al., 2008). This E-W model crosses the main fumarolic areas of Bocca Grande (BG), Pisciarelli (P), and the Fangaia mud pool (F).

3. Material and Methods

3.1. Electrical Resistivity Tomography: Acquisition Processing and Inversion

During each ERT measurement, an electric current is injected into the ground between two current electrodes (A, B). This current generates an electrical field. The resulting electrical potential distribution is sampled between two voltage electrodes (M, N). Transfer resistance R (in Ω) is then calculated using Ohm's law: $R = \Delta V/I$, where ΔV denotes the electrical potential difference between M and N and I is the injected current between the current electrodes A and B.

In order to characterize the subsurface electrical conductivity of the Solfatara volcano, 73,987 transfer resistances were collected along 63 ERT profiles between 2008 and 2016. (Surveys information in Table S1 and the reliability of data with time are investigated in Text S2.) We performed 14 profiles crossing the crater rim and the main faults (Figure 1b). The density of the measurements was increased around the two major hydrothermal areas corresponding to the Bocca Grande fumarole and the Fangaia mud pools. Electrode spacing varies from 2 m on dense profiles, to 10 m and 20 m for the 0.95 km and 1.26 km long profiles, respectively. For each ERT profile, we used either the Wenner or the Wenner-Schlumberger arrays because of their good signal-to-noise ratio. In addition, pole-pole and gradient configurations were realized on several profiles for a greater depth of investigation and a quick acquisition time, respectively.

Electrode coordinates were obtained using a real-time kinematic Global Positioning System (GPS) with 2 cm accuracy. On some remote locations, a handheld GPS with a 2 m precision was used. Electrode elevations were recovered after a linear interpolation using a precise 1 m resolution digital elevation model (DEM) to ensure a common elevation baseline for all electrodes.

Each transfer resistance value was obtained by stacking three to seven individual measurements. Only measurements with a standard deviation below 5% were retained for the inversion. Furthermore, it appeared that in the globally conductive area of the Solfatara crater, an injection current below 50 mA was not high enough to ensure robust resistance measurements; consequently, we removed these data. At the end of the filtering process, 43,432 transfer resistance were kept for the inversion.

An unstructured mesh of the Solfatara volcano was constructed with 902,919 tetrahedral elements and 180,211 finite-element nodes using TetGen algorithm (Si, 2015). The mesh was delimited by electrical

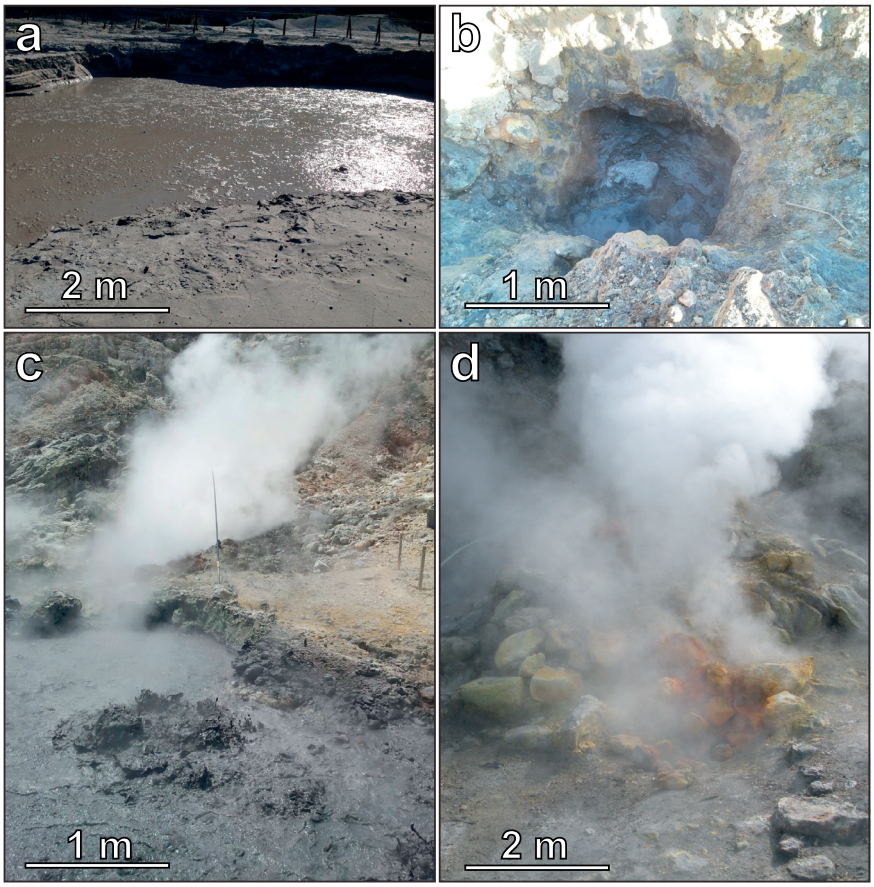

Figure 3. Hydrothermal manifestation at the Solfatara volcano: (a) the Fangaia mud pool, (b) the "Nuova Fangaia," (c) the Pisciarelli fumaroles with mud pool, and (d) the Bocca Grande fumarole. These mud pools are identified with green stars in Figures 5, 6, S2, and S4, and fumaroles are shown with black circles.

resistivity surveys and covers a ~0.68 km^2 ovoid area. The surface topography was integrated using the 1 m accuracy DEM (Figure S1). Mesh refinement was achieved near the electrodes location to improve the numerical accuracy (Johnson et al., 2010). In addition, five specific domains were defined to apply either distinct inversion options or a specific mesh refinement depending on the measurements density. The bottom of the mesh was set to 50 m below sea level (bsl), based on the maximum depth investigation reached by the 1.26 km long ERT surveys. Finally, an external domain was created by extending the mesh 20 km both laterally and at depth to avoid boundary effects.

The inversion of the electrical conductivity was performed using the E4D inversion code (Johnson et al., 2010). Regularization was done using classical first-order isotropic spatial derivative with deterministic smoothing constraints. Solving the inverse problem consists in minimizing the Occam's type objective function:

$$\Phi = \Phi_d\,(\boldsymbol{u_d}) + \beta\Phi_m(\boldsymbol{u_m}), \tag{1}$$

with $\boldsymbol{u_d}$ and $\boldsymbol{u_m}$ given by:

$$\boldsymbol{u_d} = \boldsymbol{W_d}\left(\boldsymbol{d}_{\text{obs}} - \boldsymbol{d}_{\text{pred}}\right), \tag{2}$$

$$\boldsymbol{u_m} = \boldsymbol{W_m}(\boldsymbol{m}_{est} - \boldsymbol{m}_0), \tag{3}$$

where $\boldsymbol{d}_{\text{obs}}$ and $\boldsymbol{d}_{\text{pred}}$ are respectively the observed and simulated transfer resistance values, $\boldsymbol{W_d}$ is a diagonal data weighting matrix, which contains the reciprocal of the standard deviations of the measurements along the diagonal, and Φ_d represents the Euclidian L2 norm of $\boldsymbol{u_d}$. In the model constraint term, $\boldsymbol{m}_{\text{est}}$ represents the estimated natural logarithm of the conductivity distribution, $\boldsymbol{m}_0$ represents a prior conductivity model, and $\boldsymbol{W_m}$ is the regularization matrix. Finally Φ_m is the Euclidian L2 norm of $\boldsymbol{u_m}$. The regularization matrix is

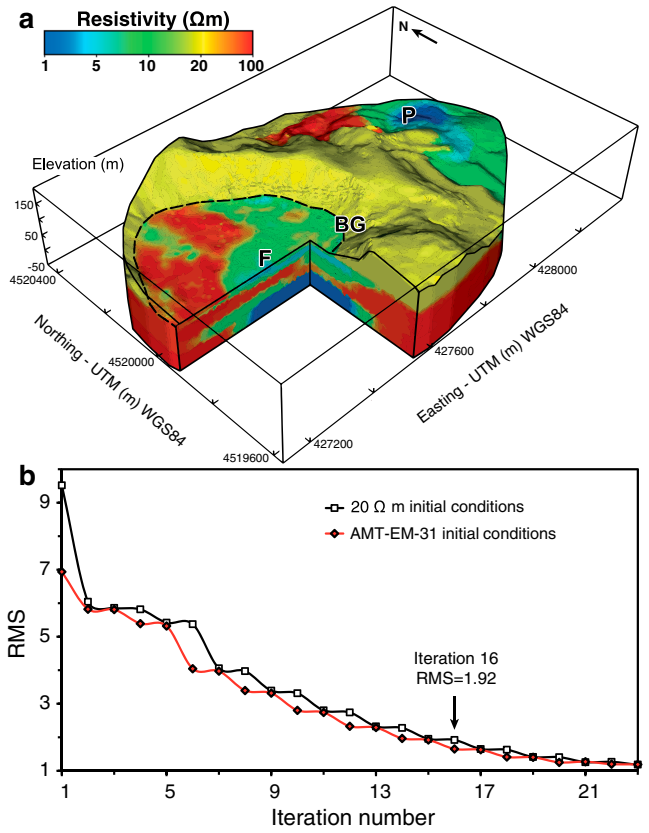

Figure 4. Inversion of ERT data. (a) Initial electrical resistivity model (Ω m) derived from the interpolation of resistivity values found from inversion of electromagnetic data on the 902,919 elements of the mesh. Surface resistivity down to 6 m is obtained after electromagnetic EM-31 data (inside the dotted line area, see Figure 4a, Text S3, and Figure S2). The deeper resistivity layers are taken from the audio-magnetotelluric surveys (AMT). In regions without AMT or EM-31 data, the resistivity has been fixed to the average value of 20 Ω m. Main locations are Fangaia pool (F), the Bocca Grande fumarole (BG), and the Pisciarelli area (P). (b) Decrease of the RMS at each iteration for the two inversions: homogeneous initial model (20 Ω m) and heterogeneous initial condition derived from AMT and EM-31 conductivity surveys with prior constraints (see Figure S3c for RMS relative comparison). The blue dotted line indicates that the AMT-EM-31 inversion has converged after 16 iterations with a RMS of 1.92. The AMT-EM-31 initial model slightly enhances the data fitting compared with the homogeneous one, especially in the earlier iterations. Consequently, we decided to present this model in the paper. However, the homogeneous model displays a similar structure but is less resolved in areas without ERT data.

formulated to impose smoothly varying structure in the inverse solution when Φ_m is minimized. The regularization parameter (or trade-off parameter) β determines how much weight is placed on minimizing Φ_m in comparison to Φ_d when minimizing the overall objective function. At the first iteration β starts at a large value, thereby imposing smoothness on the solution. As the inversion progresses, β is systematically reduced to enable reduction in Φ_d(i.e., to improve the data fit) by allowing greater heterogeneity in the resistivity distribution. By default, the β value is conservatively decreased by half of its previous value when the total objective function Φ decreases by less than 5% compared to the previous iteration. At each iteration, data points whose weighted residual error exceeds three standard deviations from the mean weighted residual error are considered as outliers and removed (Figure S3b). Note that outliers are defined at each iteration, which means that removed values can be reused in the next iteration. If the data are appropriately weighted, the inversion converges when the normalized χ^2 statistic (i.e., the squared RMS) reaches 1:

$$\chi^2 = \frac{1}{N}\sum_{i=1}^{N}\left(\frac{d_{\mathrm{pred},i} - d_{\mathrm{obs},i}}{\sigma_i}\right)^2, \tag{4}$$

where N is the total number of transfer resistance data and σ_i is the standard deviation of the transfer resistance given by the following criteria proposed by LaBrecque and Yang (2001):

$$\sigma_i = M\, d_{\mathrm{obs},i} + \gamma. \tag{5}$$

Here $M = 0.05$, is a 5% error set for all data while $\gamma = 0.001$ Ω is considered as the instrument precision and prevents measurements with excessively small transfer resistance magnitudes from dominating the inversion. We used $M = 5\%$ because (1) filtered data standard deviations are often lower than forwarding modeling errors, such that forward modeling errors determine the appropriate convergence criteria, and (2) forward modeling errors are typically no more than 5% of transfer resistance magnitude. Under these assumptions, the data may be slightly underfit when $\chi^2 = 1$ but not overfit and, therefore, free from overfitting induced artifacts.

The ERT inversion is a highly non unique problem unless Occam's type-regularization is used to constrain the solution (Loke & Barker, 1996). Hence, additional constraints and a priori information have to be implemented to better constrain the subsurface structure (Doetsch et al., 2012; Johnson et al., 2012; Zhou et al., 2014). We incorporated two prior constraints. First, the electrical conductivity of water in the Fangaia mud pool is regularly measured around 1 S m^{-1}. Hence, we defined a small mesh domain according to the spatial extent of this liquid area (70 m^2, 2 m deep) and then fixed its electrical conductivity value during the inversion process (Johnson et al., 2012). In addition, a prior conductivity distribution was used as a starting model. It was obtained by interpolation of the 3-D resistivity model from audio-magnetotellurics (AMT) data inversion with a spatial resolution of ~50 m (Figure 4a and Text S3). These electromagnetic data were combined with a conductivity model, for the six first meters, derived from an EM-31 apparent conductivity data (Text S3 and Figure S2). In regions where no AMT or EM-31 data were available, the electrical resistivity was assigned to a value of 20 Ω m corresponding to the mean resistivity value of the 63 tomograms. As stated before, the convergence criterion of the inversion is given by a target value of the normalized chi-square in equation (4), which was determined assuming modeling errors are greater than measurement errors. After viewing the inversion results at each iteration, and as an extra precaution against over fitting the data, we opted to terminate the inversion before the normalized chi-square reached unity. Under these conditions, the 3-D resistivity model of the Solfatara converged after 16 iterations, with a RMS of 1.92 (Figures 4b and S3).

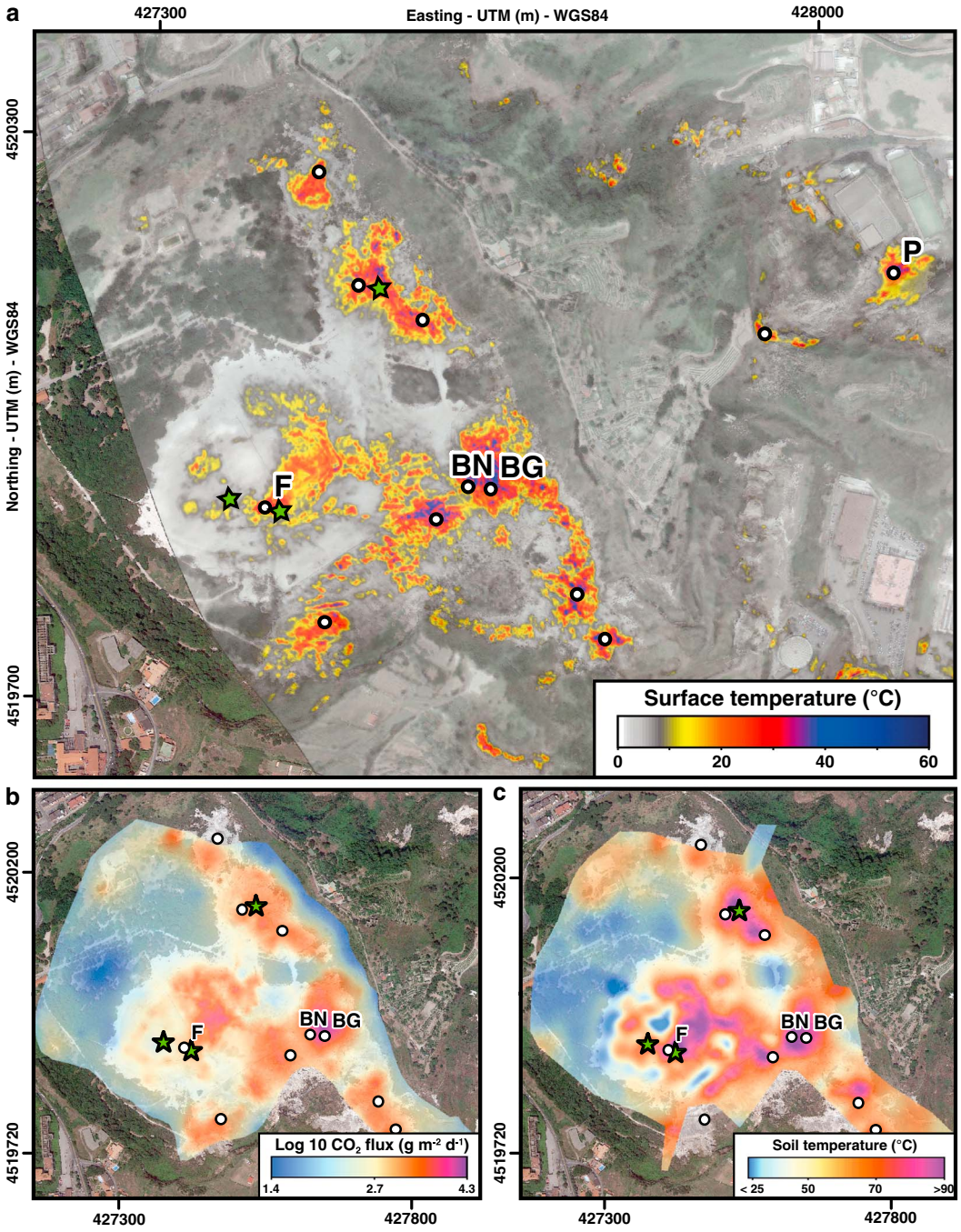

Figure 5. Solfatara satellite image (2014) draped with (a) surface infrared thermal image (°C), (b) soil CO_2 flux (g m^{-2} d^{-1}), and (c) soil temperature (°C) at 30 cm depth. These values were interpolated using a geostatistical ordinary kriging method (isotropic Gaussian semivariogram model). Main vents are indicated with black circles: Bocca Grande (BG) and Bocca Nuova (BN) fumaroles, and the Fangaia mud pool (F). Location of surface liquid water is represented with green stars.

3.2. Temperature and CO_2 Flux Mapping

An infrared thermal image of the Solfatara crater and its surroundings was captured, using an Airborne Multispectral sensor Daedalus 1268 ATM Enhanced (Borfecchia et al., 2013) on 19 December 2013, 04:00 (UTC). We orthorectified and georeferenced this 1 m ground resolution image with 70 benchmark points (Figure 5a).

Soil CO_2 flux measurements were carried out using the accumulation chamber method (Chiodini et al., 1996) with an infrared gas analyzer LI-COR LI 800. Reproductibility of field measurements is around 10%

(Chiodini et al., 1998) and CO_2 saturation value of the detector is 20,000 ppm. The data set includes 1,136 measurements that were interpolated using a geostatistical ordinary kriging method (isotropic Gaussian semivariogram model) to provide a mapping of soil diffuse CO_2 flux. In addition, we collected 2,085 soil temperatures at 30 cm depth using a thermal probe (K thermocouple) and used the same geostatistical process to produce a soil temperature map (Figures 5b and 5c). Since both CO_2 flux and temperature surveys were collected between 2008 and 2016, we investigated their reliability with time which showed no significant changes of the main anomalies over the years (Text S2).

3.3. Soil pH and CEC Measurements

Accurate interpretation of self-potential signals (Text S1) and electrical resistivity in terms of geological structures, fluid, or clay content requires the knowledge of petrophysical properties. To this end, we performed soil measurements of CEC and pH on 27 representative samples inside the Solfatara crater (Figure 6).

In situ soil pH measurements followed the protocol detailed by (Hendershot et al., 2008) using a Woltcraft pH meter PHT-01 ATC. In practice, 10 g of soil are added into a beaker with 50 mL of deionized water. The suspension of soil is stirred intermittently for 30 min and left to rest 1 h. Finally, pH measurement is realized on the supernatant.

The CEC was determined following the method proposed by Aran et al. (2008). We adapted the protocol in order to keep a good precision and reproducibility for low values ($<$2 meq 100 g^{-1}). For this purpose, we increased the soil mass from 2 to 10 g and decreased the cobaltihexamine chloride concentration from 0.05N to 0.01 N. In practice, 10 g of dry soil are added into a propylene tube with 40 mL of 0.01 N cobaltihexamine chloride solution. After 1 h of shaking, supernatant is filtered on a 0.22 μm. Finally, absorbance is measured at 472 nm using a spectrophotometer. CEC is calculated with the following formula:

$$\mathrm{CEC}_{\mathrm{A472}} = \left[\frac{\left(\mathrm{A472}_{0.05\mathrm{N}} - \mathrm{A472}_{\mathrm{sample}}\right)}{\mathrm{A472}_{0.05\mathrm{N}}}\right] \times 10 \frac{V}{m} 100, \tag{6}$$

where $A472_{0.05N}$ and $A472_{sample}$ are the absorbencies at 472 nm of 0.01 N cobaltihexamine chloride solution and of sample supernatant respectively, V is the volume (L) of cobaltihexamine chloride solution added to soil sample and m is the weighed dry soil (g). Measurements deviation was tested with five measurements on two samples, and differences were lower than 10%.

4. Results

4.1. Main Degassing Structure Imaged by the Ground Temperature and Soil CO_2 Flux Mappings.

The surficial extent of the Solfatara hydrothermal zone is well delimited on the maps of diffuse soil CO_2 flux and ground temperature, showing a clear spatial correlation (Figure 5). The main temperature and flux anomalies ($T >$ 40°C, at 30 cm depth and soil CO_2 flux $>$500 g m^{-2} d^{-1}) are clustered inside the Solfatara crater and on its eastern flank, near Pisciarelli (Figure 5a). This diffuse degassing structure (Chiodini et al., 2001) of ~0.5 km^2 area coincides with the main SW-NE and N-S regional faults. This degassing activity leads to strong hydrothermal alteration with the formation of secondary minerals (Mayer et al., 2016). In this region, alteration results in a whitish to reddish color of the ground and the lack of any vegetation. The diffuse degassing structure can be subdivided in three main parts:

1. diffuse degassing area in the central part of the crater, at the Solfatara cryptodome and around main fumaroles with intense soil CO_2 flux from ~1,000 up to ~20,000 g m^{-2} d^{-1}. The ground temperature (at 30 cm depth) can reach 98°C, which is close to the boiling temperature.
2. direct intense degassing at the main fumaroles: Bocca Grande (~164°C, ~150 t d^{-1} of CO_2), Bocca Nuova (~148°C, ~50 t d^{-1} of CO_2), and Pisciarelli (~115°C, ~300 t d^{-1} of CO_2 after Aiuppa et al., 2013). These vents lie on ring and buried faults after Isaia et al. (2015).
3. mud pools, where CO_2 and steam are bubbling through hot water (from 50 to 90°C), marked by green stars in Figure 5. They are located inside the crater at the Fangaia but also close to the Solfatara cryptodome and at the Pisciarelli fumarole (Figure 3).

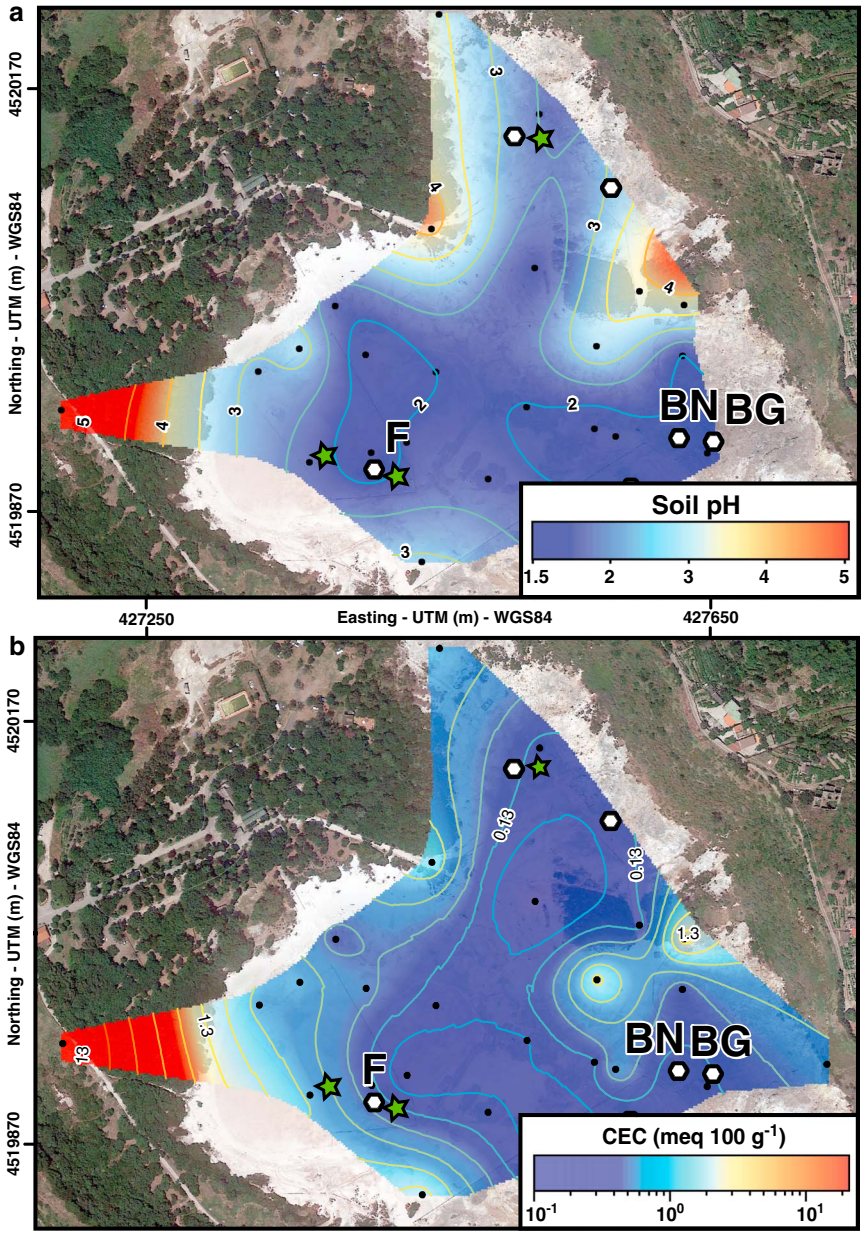

Figure 6. Solfatara satellite image (2014) draped with a mapping of (a) soil pH and (b) CEC values (meq 100 g^{-1}) for the 27 soil samples (black dots). These values were interpolated using geostatistical ordinary kriging method (isotropic Gaussian semivariogram model). Main vents are indicated with black circles: Bocca Grande (BG) and Bocca Nuova (BN) fumaroles, and the Fangaia mud pool (F). Location of surface liquid water is represented with green stars.

4.2. Petrophysical Investigations

Maps of soil CEC and pH are shown on Figure 6. These parameters are correlated and display very low values (CEC $<$ 1 meq 100 g^{-1} and pH $<$ 2.5) inside the crater, with minimum values in the Fangaia mud pool and close to the main fumaroles. Highest values (CEC $>$ 5 meq 100 g^{-1} and pH $>$ 3) are located in vegetated areas and mainly related to the presence of organic matter, clearly visible in these samples.

4.3. Three-Dimensional Resistivity Model of Solfatara

The 3-D resistivity model of the Solfatara crater and Pisciarelli is characterized by low values ranging from 1 to 150 Ω m and thus appears as globally more conductive than other volcanic edifices (Byrdina et al., 2017; Revil et al., 2011, 2010; Rosas-Carbajal et al., 2016). The observed resistivity range is in good agreement with

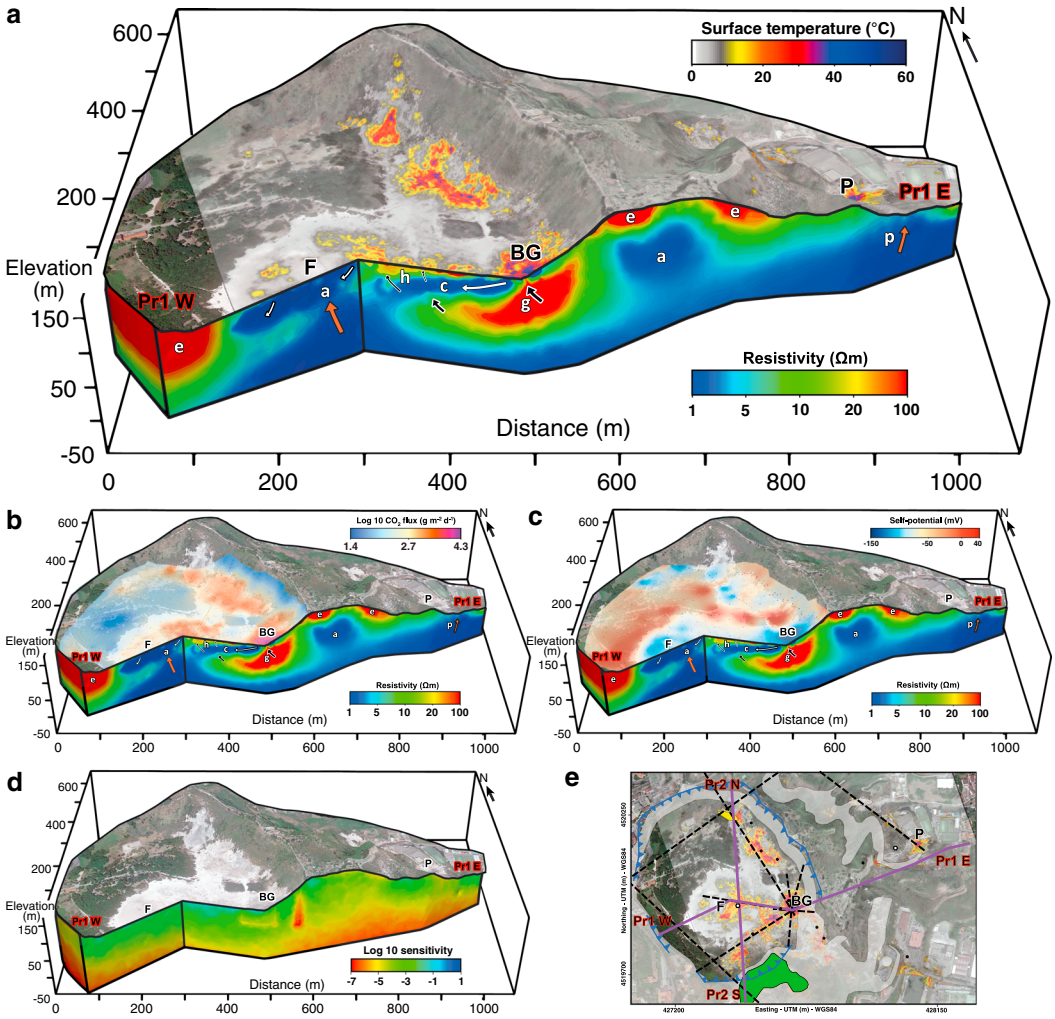

Figure 7. Resistivity cross section Pr1 overlapped with (a) surface temperature image (°C), (b) soil CO_2 flux (g m^{-2} d^{-1}), (c) self-potential (mV) mapping (black dots indicate the measurements location), (d) sensitivity of the 3-D cross section. Pr1 crossing the Fangaia pool (F), the Bocca Grande fumarole (BG), and the Pisciarelli area (P). Principal units are "g" = gas-dominated reservoir with a thin conduit toward Bocca Grande, "p" = liquid-dominated plume, "c" = area of formation, and circulation of condensate, "e" = eruptive deposits (see results section for explanations), orange arrow = convective plume, black arrow = gas flow, and white arrow = liquid-dominated flow, and (e) location of the two resistivity cross sections, Pr1 and Pr2 (purple lines) on satellite image overlapped with geological map presented in Figure 1b.

previous 2-D ERT studies (Bruno et al., 2007; Byrdina et al., 2014; Isaia et al., 2015) and 2-D AMT surveys performed at Solfatara (Troiano et al., 2014). It is also consistent with borehole resistivity measurements carried out in the Campi Flegrei caldera (Giberti et al., 2006; Rabaute et al., 2003). The sensitivity of our model is satisfactory down to 150 m below the surface (50 m bsl) in the center of the crater and to 100 m below the surface (sea level) on outer edges and at Pisciarelli. Beneath sea level, the whole structure is conductive, with electrical resistivity <5 Ω m, in good agreement with the AMT model. This low resistivity structure is mostly related to ERT surveys. However, in areas that are not covered by these surveys (e.g., N-E of the volcano), the AMT resistivity model provides additional constraints at depth, whereas the EM-31 resistivity model brings a minor contribution in the shallow subsurface of the crater. Thanks to very high density measurements (43,432 points expanded on ~0.68 km^2), the model resolution at shallow depths reaches 1–2 m in the main fumarolic area, 4 m at the Fangaia, and 10 to 20 m close to the long ERT profiles.

To support our results, we present cross sections of the 3-D resistivity model, overlain with maps of temperature, soil CO_2 flux, self-potential (from Byrdina et al., 2014) and 3-D representations of electrical resistivity isovalues. Two resistivity cross sections are shown in Figures 7 and 8 together with a surface temperature

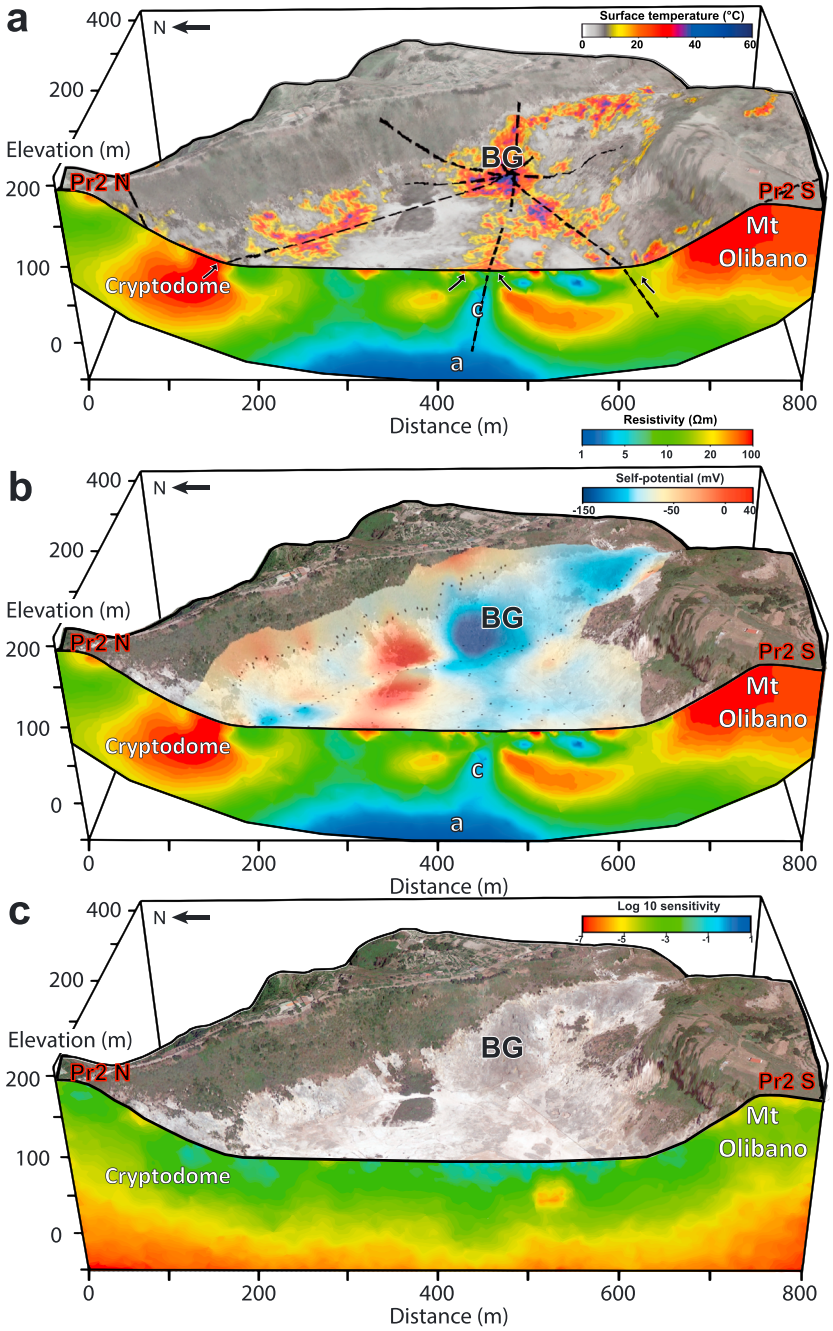

Figure 8. Resistivity section Pr2 (see Figure 7e for location), crossing from north to south the Solfatara cryptodome and Mount Olibano draped with (a) surface temperature (°C) and (b) self-potential (mV) maps (black dots indicate the measurements location). Principal units are "a" = liquid-saturated, and or clay-rich area, "c" = area of formation, and circulation of condensate, "g" = gas-dominated reservoir; black arrow = gas flow, and white arrow = liquid-dominated flow. Black dotted lines indicate at the surface the main faults/fractures (as in Figure 1b) and their prolongation at depth. The sensitivity of the 3-D cross section is represented in Figure 8c.

image, soil CO_2 flux, and self-potential. The Pr1 cross section is roughly W-E oriented, 1.2 km long, and passes through the main structures as the Fangaia mud pool, the hummocks area, the Bocca Grande fumarole, then finally crosses the Solfatara eastern rim and reaches the Pisciarelli fumarole. The Pr2 cross section is N-S oriented, 800 m long, and crosses the Solfatara cryptodome, the hummocks area, and finally the Mount Olibano lava dome. Location of the two resistivity cross sections, Pr1 and Pr2, are represented by purple lines in Figure 7e together with the geological map after Isaia et al. (2015). Both cross sections have an investigation depth of 150–200 m below the surface. The corresponding electrical resistivity sensitivity

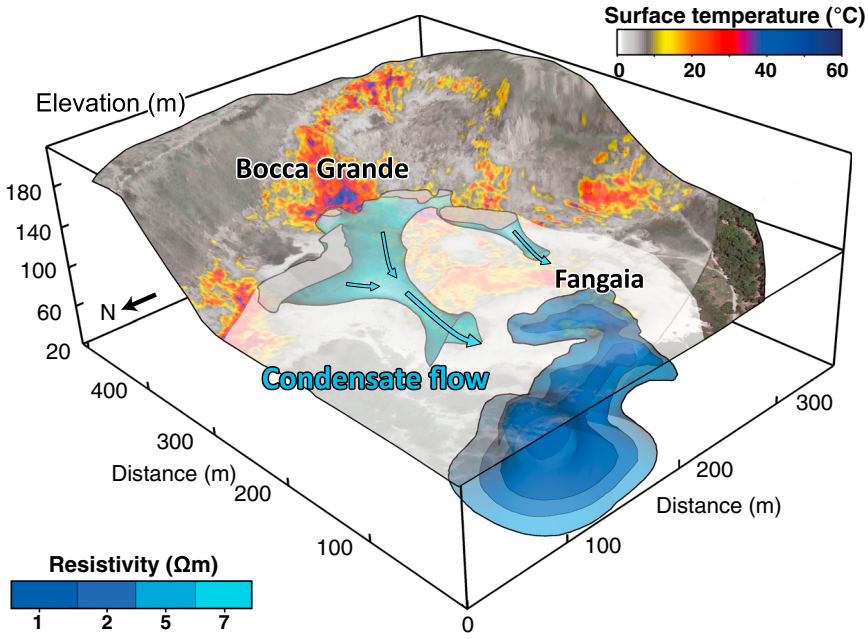

Figure 9. Surface temperature (°C) map of the Solfatara crater with several 3-D electrical resistivity isovalues. The 7 Ω m isovalue in light blue indicates the condensate flow ("c" unit) that originates from main hot degassing areas, and flows toward the Fangaia mud pool. The Fangaia liquid-dominated plume is represented with three blue isovalues from 1 to 5 Ω m and highlights the conical plume shape feeding the mud pool.

maps are shown in Figures 7d and 8c. The sensitivity is optimal around the Bocca Grande fumarole with values higher than 10^{-3}. For values below 10^{-6}, the resistivity model can be considered as poorly constrained, and consequently, the resistivity cross section has been cut out according to this threshold.

4.4. Hydrothermal Structures

Our resistivity model highlights several hydrothermal structures denoted by lowercase letters in Figures 7 and 8. The cross section Pr1 shows a resistive structure of 20–40 Ω m labeled "g" (as gas dominated). This unit is located 60 m beneath the Bocca Grande fumarole and is directly connected to the vent by a ~10 m thick resistive channel. On the same profile, the Fangaia mud pools and Pisciarelli are both imaged as conductive bodies. At Pisciarelli, a conductive "p" unit (as plume) of 5–10 Ω m reaches the surface on the eastern flank of the Solfatara crater. It is located in a high diffuse degassing area, near the Pisciarelli vent (Figure 3c). The Fangaia mud pool area appears as the most conductive region within the Solfatara crater, with resistivity ranging between 1 and 5 Ω m, and is denoted by "a" (as Fangaia aquifer). At its surface, a 5 Ω m conductive layer extends over ~400 m^2 and surrounds hot acidic mud pools. We used isovalues of electrical resistivity to image this 3-D structure beneath the Fangaia (Figure 9). It reveals a fairly symmetrical conical shape enlarging at depth toward the northwestern side, whose resistivity values progressively decrease in the central part and at depth reach a minimal value of 1 Ω m. On Pr1, a 1–10 Ω m inclined layer labeled "c" (condensate flow) lies between the Bocca Grande fumarole and the Fangaia. Using a 7 Ω m resistivity isovalue, we delineate a ~20-m-thick cylindrical channel sloping toward the Fangaia. This "c" unit is also connected to two other intense degassing areas in the inner east and south crater flank (Figure 9).

Comparing the resistivity tomograms with the geological map (Figure 10a) allows us to distinguish two volcanic structures presented in Pr2 and Pr1 cross sections. The first resistive structure of 50–150 Ω m is located in the S-SE part of the Solfatara crater on Pr2 (Figure 8) and corresponds to the ancient Mount Olibano lava dome. The latter extends from the surface down to 50 m bsl, at the bottom boundary of the model. Thermal anomalies are observed in the northern part of Mount Olibano, where there are buried faults. A second structure, with similar electrical resistivity values (50–100 Ω m), is found in the N-E part of the crater on Pr2 and represents the shallow part of the Solfatara cryptodome (Isaia et al., 2015).

On Pr1, an intermediate resistivity structure (20–50 Ω m) of ~30 m thickness, labeled "e" unit (eruptive deposits), lies on the top of the crater rim and vegetated areas (Figures 7 and 10). This region does not display any

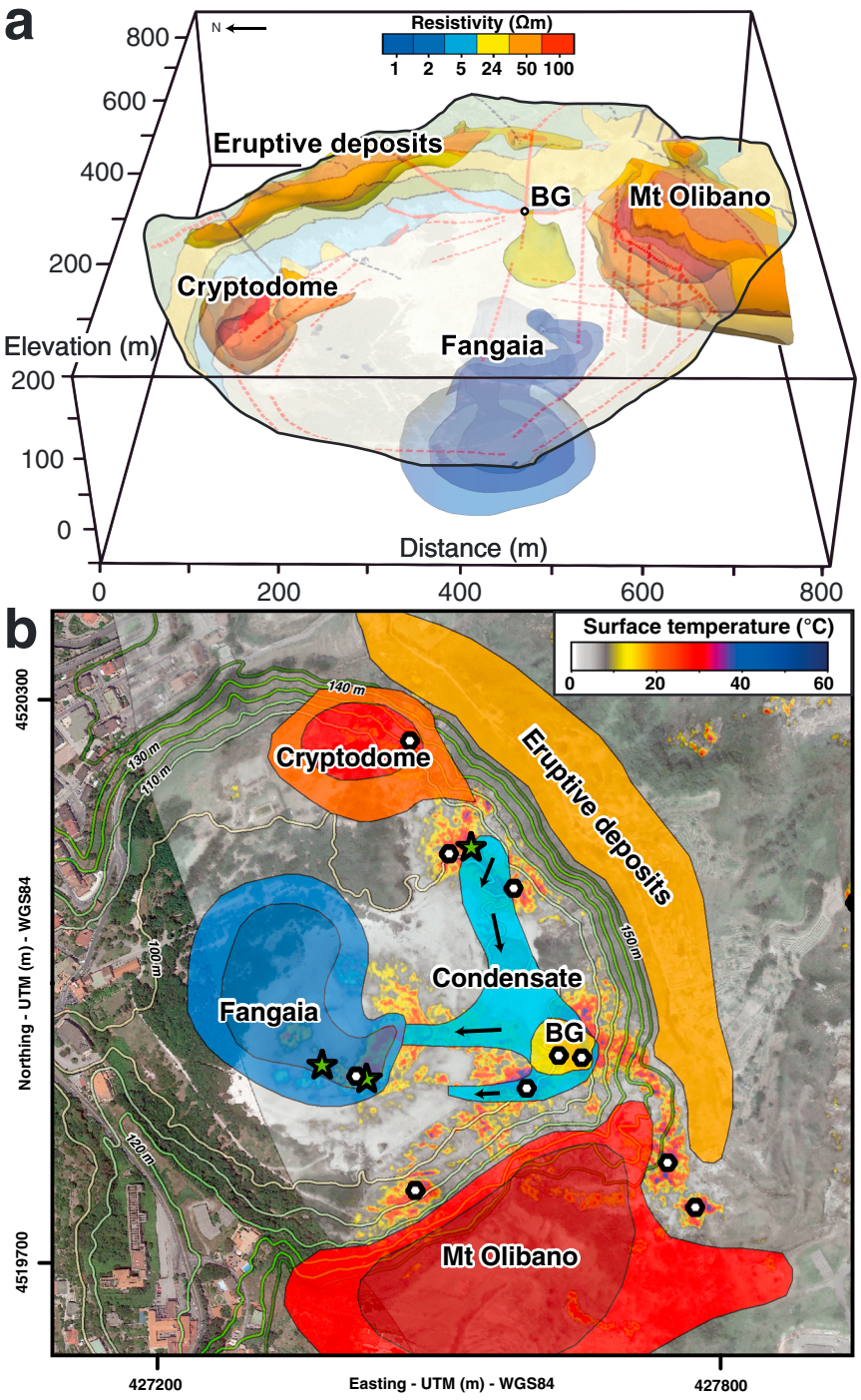

Figure 10. Extent of the main electrical resistivity isovalues at the Solfatara crater compared with, (a) the 3-D geological map, after Isaia et al. (2015), and (b) surface infrared thermal image (°C) with the electrical resistivity isovalues projection. The main resistivity structures are Solfatara cryptodome, Mount Olibano (50–150 Ω m, orange red), eruptive deposits (20–50 Ω m yellow orange), and hydrothermal structures: gas-dominated reservoir feeding the Bocca Grande fumarole (24 Ω m, yellow), condensate flow (7 Ω m light blue) and Fangaia mud pool plume (1–5 Ω m, blue). Main vents are indicated with black circles: Bocca Grande (BG) and Bocca Nuova fumaroles, as well as the Fangaia mud pool. Location of surface liquid water is represented with green stars.

thermal or gas flux anomalies but clearly corresponds to the recent Solfatara and Astroni tephra deposits (Isaia et al., 2015). Two movies slicing the 3-D electrical resistivity model from west to east, and as a function of depth, are available in the supporting information (Movies S1 and S2). Both movies are combined with the surface temperature map of the crater.

5. Discussion

5.1. Alteration and Low Resistivity at the Solfatara Crater

Geology at Solfatara is mainly composed of tephra deposits and ancient lava domes (Isaia et al., 2015; Petrosino et al., 2012). These two types of volcanic materials generally display distinct resistivity signatures. For instance, at Vulcano and Stromboli volcanoes, the electrical resistivity of massive lava ranges between 2,000 and 5,000 Ω m, which is 1–2 orders of magnitude higher than the tephra deposits one measured on the same volcanoes (Finizola et al., 2009; Revil et al., 2008). Here we observe lower electrical resistivity values (50–150 Ω m) at the Solfatara cryptodome and Mount Olibano lava dome, which can probably be explained by the presence of fluids, and possibly be associated to host rock hydrothermal alteration. Indeed, the Solfatara crater has been hosting a sustainable hydrothermal system for the last ~4,000 years without eruptions (Isaia et al., 2009). Chemical weathering and leaching produced by the circulation of hot acid hydrothermal fluids, and meteoric water infiltration, are well-known processes with the capacity to almost completely alter volcanic rocks (e.g., Keller, 1980; Thien et al., 2015).

5.2. Resistive Gas-Dominated Reservoir Feeding Bocca Grande Fumarole

The resistive "g" structure of 20–40 Ω m, is located at 60 m below the Bocca Grande fumarolic area (Figures 7a and 10a) and intersects several faults at the Bocca Grande vent (Figure 8a), where soil temperature and soil CO_2 diffuse degassing are very high (>98°C and >15,000 g m^{-2} d^{-1}, respectively). We suggest that it represents a gas-dominated reservoir feeding the Bocca Grande fumarole, for the following reasons:

1. The depth of "g" unit is consistent with vapor-dominated conditions, considering a hydrostatic pressure at its top (6 bars) with a temperature larger than the vent (165°C).
2. The higher resistivity of this unit can be explained by the presence of steam in a porous medium, as the resistivity depends on fluid saturation of pore space (Milsch et al., 2010; Roberts et al., 2001). Indeed, we calculated an increase of electrical resistivity from ~1 Ω m to 24 Ω m, when pore liquid fluid is substituted by a partial gas -saturation at 165°C (see Text S4).
3. A ~10 m thick resistive channel directly connects the gas-dominated reservoir to the vent. This conduit could be a fluid-filled fracture discharging at Bocca Grande fumarole. It is important to note that due to the dense ERT measurements in this area, the model resolution is sufficiently high to resolve this channel (Figure 7d).
4. The minimum of self-potential distribution in the crater (−150 mV) is correlated with the Bocca Grande fumarole (Figures 7c, 8b, and S4). Here these negative streaming potential anomalies at fumaroles and the Fangaia mud pools are explained by a positive zeta-potential (Revil & Pezard, 1998) (Text S1), as the soil shows acidic pH (<2) (Figures 6a and S4). Hence, in this case, an upwelling of fluids can generate negative self-potential values.

Using 2-D ERT surveys, Byrdina et al. (2014) recognized a resistive body underneath the Bocca Grande fumarole, as well as Troiano et al. (2014) with MT soundings (a comparison between MT and ERT models is presented in Figure S5). We confirm this structure to be a gas-dominated reservoir as our present 3-D model is able to prove its connection to Bocca Grande fumarole (Figure 7). The location of the conduit is consistent with the maximum soil temperature, CO_2 flux, and negative self-potential anomalies. The volume of this vapor-dominated reservoir can be estimated to be around 25,000 m^3 using the 24 Ω m resistivity isovalue (see Text S4). According to Fournier (2006), gas-dominated regions are underpressurized with respect to the local hydrostatic gradient. Thus, a narrow low-permeability "barrier" is needed at the top of the gas reservoir to separate the vapor static from the hydrostatic overlying region (Ingebritsen & Sorey, 1988), as observed in this study.

5.3. Channel of Condensate Water Inferred from Electrical Resistivity

Although the emitted gas is mainly released into the atmosphere, a significant part of steam condenses at the Solfatara crater (few thousands of tons) when approaching the surface, due to atmospheric cooling (Chiodini et al., 2004). The presence of water at the surface is obvious at the Fangaia mud pool and at the Pisciarelli fumarole and was recently observed in the inner N-E side of the crater (Figure 3b). Interestingly, no observations of such condensed water have been ever identified, so far, in Bocca Grande area. However, lying between the resistive gas-dominated reservoir "g", and the surface, a conductive "c" unit (1–10 Ω m) could represent a liquid-saturated layer formed by steam condensation. It should be noted that for a given

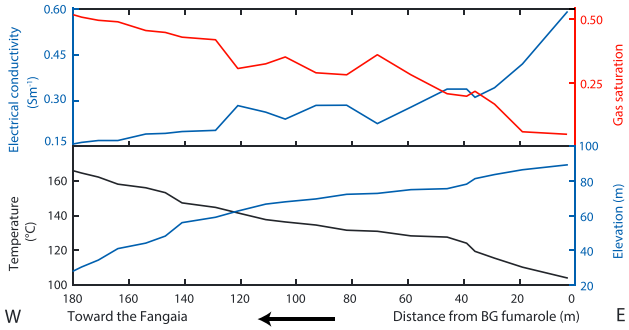

Figure 11. Change in gas saturation along the condensate unit "c" shown in Figures 7, 9, and 10 calculated from the electrical conductivity of the model assuming the temperature follows the saturation temperature curve versus depth (see section 5.3 for explanations and Text S4 for equations).

temperature, the conductivity of this "c" unit can be attributed to either surface conductivity or fluid saturation and salinity.

Here the very low soil CEC values (<2 meq 100 g^{-1}, Figure 6b) measured in the crater prove the surface conductivity represents a minor contribution with respect to the fluid conductivity. According to the power law relationship between CEC and surface conductivity (Revil et al., 2017b), the CEC of the "c" unit corresponds to surface conductivities lower than 10^{-3} S m^{-1}. This value is 1 or 2 orders of magnitude lower that the measured electrical conductivity at the Solfatara (10^{-2} S m^{-1} up to 1 S m^{-1}). Consequently, the low resistivity values of the "c" unit cannot be directly attributed to high-surface conductivity.

The absence or the low content of such clay minerals was already attested at the Solfatara crater (Mayer et al., 2016; Zimbelman et al., 2005). Indeed, in very acidic environments (pH < 2), such as the Bocca Grande fumarole and the Fangaia mud pool (Figure 6a), the formation of conductive clays is limited or does not take place, the alteration products being rather alunite and amorphous silica (Zimbelman et al., 2005). Hence, we demonstrate here that the shallow resistivity variations of the central zone of the Solfatara crater are essentially related to fluid content and temperature changes.

Consequently, we suggest that electrical resistivity contrasts between "g" and "c" units are related to a sharp phase transition between a vapor-dominated area and a liquid-saturated zone. In absence of surface conductivity, the minimum electrical resistivity calculated for a full water saturation of tuff rocks at 105°C is about ~2.5 Ω m (see Text S4). The resistivity observed near the Bocca Grande fumarole is consistent with this value (Figure 7). By choosing a higher resistivity (7 Ω m) as an isovalue of its boundaries, we highlight the shape of a pipe-like structure channelizing the condensate (Figure 9). This channel, of ~30% slope, drives the condensed water produced in the vicinity of the hottest degassing areas toward the Fangaia mud pool (Figure 10b). Interestingly, the channel is precisely oriented along a NW-SE buried fault inferred by Isaia et al. (2015) (Figure 8a), taking advantage of this high-permeability zone.

In order to study the condensate flow evolution along this channel, we extracted the "c" unit resistivity values from the Pr1 resistivity cross section (Figure 7). Results show the electrical resistivity increases as the condensate flows downward to the Fangaia (Figure 11). Therefore, to investigate if these resistivity variations could be due to an increase of temperature and gas content along the path, we have calculated the gas saturation associated to the extracted electrical resistivity values (equations given in Text S4), considering the following assumptions: (i) The fluid inside the condensed channel "c" is characterized by saturation temperature of water (considering hydrostatic pressure) due to the buffering effect of steam present at boiling point. This hypothesis is physically necessary to explain a two-phase region indirectly inferred previously and (ii) the tuff properties remain homogeneous along the "c" units.

Near the Bocca Grande fumarole, results indicate that the condensate flow (at 105°C) is liquid saturated. Then, gas proportion increases in the downward channel to reach a saturation value of 0.5, close to the Fangaia. This increase in gas saturation together with the high diffuse soil CO_2 flux measured at the surface (Figure 11) likely indicates that hot gases percolate through the channel. In addition, self-potential measurements along the profile show a decrease from the Bocca Grande area (−110 mV) toward the Fangaia (−80 mV). This positive variation of 30 mV is interpreted as a downward fluid flow from the Bocca Grande fumarole to the Fangaia.

5.4. Hummocks Structures

In the central region of the crater, several hummocks ("h" units) are characterized by high temperature and soil CO_2 flux (>80°C and >5,000 g m^{-2} d^{-1} respectively, Figures 7a and 7b). An intense hydrothermal alteration has been identified in this area by Mayer et al. (2016), with formation of a thin (few centimeters thick) layer of secondary minerals, including alunite and amorphous silica. The secondary mineralization, due to self-sealing processes, leads to a decrease of the permeability, which in turn impedes the degassing. This interpretation is confirmed by field observations: when a hole created by an electrode crosses this narrow impermeable layer (usually a few centimeters are necessary), a small fumarole appears and lasts a few

hours, suggesting that a certain amount of gas was trapped at a shallow depth below alunite layers. Therefore, we suggest that the intermediate electrical resistivity values observed within the hummock unit (25–70 Ω m) are related to a partially gas-saturated porous rock. Since this resistive area is also the site of the main thermal and soil CO_2 flux anomalies, we suggest a positive correlation between the presence of impermeable secondary minerals and gas-saturated area.

5.5. The Fangaia Plume

The Fangaia mud pool collects distinct sources of condensed and meteoric water. First, the condensate flow is mainly produced at the Bocca Grande fumarolic area, but it also originates from the Fangaia area itself, caused by high diffuse degassing. Second, rainwater flows inside the Solfatara crater and carries altered deposits which converge in the Fangaia topographical depression. Over time, this last process has created a flat area characterized by the lowest soil permeability identified inside the volcano (10^{-15} to 10^{-16} m^2). The presence of altered deposits at Fangaia raises here the question about the origin of low electrical resistivity values (<5 Ω m). A liquid-saturated plume was proposed by Byrdina et al. (2014) to explain such values; however, the statement whether electrical resistivity is associated either to clay or to fluid content was not really assessed. New evidences clearly characterize the Fangaia mud pool as a liquid-dominated plume. Indeed, the negative self-potential anomalies demonstrate the upwelling of fluids (Figure 7). Moreover, the 3-D conical shape of the Fangaia mud pool (Figure 9) perfectly matches the mud pool location, high soil temperature and diffuse CO_2 flux area (>50°C and >5,000 g m^{-2} d^{-1}, respectively). The electrical conductivity of the mud pool water (~1 S m^{-1}) is comparable with the values observed in the central part of the conical structure. This conductive area cannot be directly related to the presence of high-surface conductivity (usually associated with the presence of high CEC-clay minerals) because of the very low CEC and pH values (0.1–0.5 meq 100 g^{-1}, and pH < 2, Figure 6). Our interpretation of a liquid plume is also consistent with results of Serra et al. (2016) who performed a 3-D active seismic tomography in the Fangaia area. The abrupt attenuation of *S* wave in the eastern part of the Fangaia was interpreted as a sharp transition between an unsaturated medium and the Fangaia liquid-saturated plume. The latter was also identified by De Landro et al. (2017) with 3-D *P* wave velocity model, and by Pilz et al. (2017) using noise-based Rayleigh and Love wave 3-D inversion. It is worth noting that the deep structure of the Fangaia conical plume is shifted to the west compared to the surface degassing structure and points to the lowest elevations of the crater rim (Figure 10b), indicating that fluid flow is driven by the topography.

5.6. Pisciarelli Area

The Pisciarelli fumarole has a lower discharge temperature than the Bocca Grande fumarole (~115°C versus ~164°C) despite its high, almost double, degassing rate. A large amount of steam condenses in this rapidly evolving fumarole of Campi Flegrei caldera (Figure 3c). Therefore, the conductive structure (5–10 Ω m) identified at depth can be interpreted as a liquid-dominated plume (Figure 7). No resistive body was found underneath the fumarole, probably because of the low resolution of the resistivity model near the Pisciarelli area (20 m interelectrode spacing) and because a temperature of 115°C is too low to form a shallow gas reservoir.

6. Conclusion

We have performed a high-resolution 3-D electrical resistivity imaging of the Solfatara volcano with 43,432 transfer resistance measurements. For the first time, we have imaged together the Solfatara crater with the Pisciarelli fumarolic area and highlighted the main geological structures, lava domes, and tephra deposits (Figure 10b). The metric resolution obtained around Bocca Grande fumarole allowed us to accurately decipher its shallow anatomy. This vent is connected through a ~10 m thick conduit to a gas-dominated reservoir at 60 m depth, whose volume can be estimated ~25,000 m^3. The intense degassing activity around the fumaroles produces a large amount of condensed water, which flows inside a buried NW-SE fault toward the Fangaia mud pool. The Fangaia and the Pisciarelli areas appear as two conductive liquid-dominated plumes where a significant quantity of water condenses, explaining the presence of mud pools.

We solved a long-discussed ambiguity concerning the nature of the shallow low conductive body below the Solfatara crater. Indeed, the low soil CEC values measured in the crater suggest a negligible contribution of surface conductivity, mainly attributed to clay-rich sediments. This interpretation is supported by low soil

pH value (<2) measured within the crater, as alteration processes cannot lead to the formation of conductive clay minerals in such an acidic environment. Hence, we conclude that the shallow variations of electrical resistivity are mainly related to fluid content and temperature.

At larger depths, from 0 to 50 m bsl, the globally conductive area (<5 Ω m) underneath the Solfatara could correspond to a clay-rich cap rock, common on geothermal areas. Indeed, in this anoxic region, H_2S cannot be oxidized into sulfuric acid. Consequently, pH values should be higher and conductive clay minerals can be formed. This conductive layer at depth could be similar to the maar-diatreme structure of the Suoana crater (Myakejima volcano, Japan) revealed by Geshi et al. (2011). In this study, authors identified an hydrothermally altered zone at 200 m below the crater that could be interpreted as a clay-rich region, as we suppose for the Solfatara crater.

The present study highlights the complex multiphase 3-D structure of the shallow Solfatara hydrothermal system. The approach used in our work is relevant to better understand the dynamics of hydrothermal systems in calderas and brings new insights into modeling and assessing the present volcanic unrest at the Campi Flegrei caldera.

Acknowledgments

Most of the computations presented in this paper were performed using the Froggy platform of the CIMENT infrastructure (https://ciment.ujf-grenoble.fr), which is supported by the Rhône-Alpes region (grant CPER07_13 CIRA), the OSUG@2020 labex (reference ANR10 LABX56), and the Equip@Meso project (reference ANR-10-EQPX-29-01) of the programme Investissements d'Avenir supervised by the Agence Nationale pour la Recherche. This research was supported by Med-Suv project. MED-SUV has received funding from the European Union's Seventh Program for research, technological development, and demonstration under the call FP7 ENV.2012.6.4-2 and grant agreement 308665. Both the data and input files necessary to reproduce the figures are available from the authors upon request (marceau.gresse@gmail.com). We sincerely thank Agata Siniscalchi and coworkers, for sharing their resistivity data obtained from a magnetotelluric survey of the Solfatara-Pisciarelli area. We are grateful to Heiko Woith from GFZ Postdam for kindly sharing electrical conductivity data of water at the Fangaia mud pool. We are also grateful to Cristian Montanaro from Auckland University, for providing us soil permeability data. The 1 m DEM used in this study was acquired thanks to a high-resolution airborne LiDAR, performed in 2009 by the Province of Naples council in the framework of the CECOSCA Project.

References

Acoccella, V., Di Lorenzo, R., Newhall, C., & Scandone, R. (2015). An overview of recent (1988 to 2014) caldera unrest: Knowledge and perspectives. *Reviews of Geophysics*, *53*(3), 896–955. https://doi.org/10.1002/2015RG000492

Aiuppa, A., Tamburello, G., Di Napoli, R., Cardellini, C., Chiodini, G., Giudice, G., … Pedone, M. (2013). First observations of the fumarolic gas output from a restless caldera: Implications for the current period of unrest (2005–2013) at Campi Flegrei. *Geochemistry, Geophysics, Geosystems*, *14*(10), 4153–4169. https://doi.org/10.1002/ggge.20261

Aizawa, K., Yoshimura, R., Oshiman, N., Yamazaki, K., Uto, T., Ogawa, Y., … Hurst, W. A. (2005). Hydrothermal system beneath Mt. Fuji volcano inferred from magnetotellurics and electric self-potential. *Earth and Planetary Science Letters*, *235*(1–2), 343–355. https://doi.org/10.1016/j.epsl.2005.03.023

Aran, D., Maul, A., & Masfaraud, J.-F. (2008). A spectrophotometric measurement of soil cation exchange capacity based on cobaltihexamine chloride absorbance. *Comptes Rendus Geoscience*, *340*(12), 865–871. https://doi.org/10.1016/j.crte.2008.07.015

Archie, G. E. (1942). The electrical resistivity log as an aid in determining some reservoir characteristics. *Petroleum Transactions of AIME*, *146*(01), 54–62. https://doi.org/10.2118/942054-G

Bechtold, M., Vilardo, G., Battaglia, M., & Orsi, G. (2005). The Campi Flegrei caldera GIS database. Retrieved from http://ipf.ov.ingv.it/cf_gis.html

Borfecchia, F., Micheli, C., Carli, F., De Martis, C. S., Gnisci, V., Piermattei, V., … Marcelli, M. (2013). Mapping spatial patterns of Posidonia Oceanica meadows by means of Daedalus ATM airborne sensor in the coastal area of Civitavecchia (central Tyrrhenian Sea, Italy). *Remote Sensing*, *5*(10), 4877–4899. https://doi.org/10.3390/rs5104877

Bruno, P. P. G., Ricciardi, G. P., Petrillo, Z., Di Fiore, V., Troiano, A., & Chiodini, G. (2007). Geophysical and hydrogeological experiments from a shallow hydrothermal system at Solfatara Volcano, Campi Flegrei, Italy: Response to caldera unrest. *Journal of Geophysical Research*, *112*, B06201. https://doi.org/10.1029/2006JB004383

Byrdina, S., Friedel, S., Vandemeulebrouck, J., Budi-Santoso, A., Suhari, W., Suryanto, M., … Kusdaryanto (2017). Geophysical image of the hydrothermal system of Merapi volcano. *Journal of Volcanology and Geothermal Research*, *329*, 30–40. https://doi.org/10.1016/j.jvolgeores.2016.11.011

Byrdina, S., Vandemeulebrouck, J., Cardellini, C., Legaz, A., Camerlynck, C., Chiodini, G., … Caliro, S. (2014). Relations between electrical resistivity, carbon dioxide flux, and self-potential in the shallow hydrothermal system of Solfatara (Phlegrean Fields, Italy). *Journal of Volcanology and Geothermal Research*, *283*, 172–182. https://doi.org/10.1016/j.jvolgeores.2014.07.010

Caliro, S., Chiodini, G., & Paonita, A. (2014). Geochemical evidences of magma dynamics at Campi Flegrei (Italy). *Geochimica et Cosmochimica Acta*, *132*, 1–15. https://doi.org/10.1016/j.gca.2014.01.021

Chiodini, G. (2009). CO_2/CH_4 ratio in fumaroles a powerful tool to detect magma degassing episodes at quiescent volcanoes. *Geophysical Research Letters*, *36*, L02302. https://doi.org/10.1029/2008GL036347

Chiodini, G., Brombach, T., Caliro, S., Cardellini, C., Marini, L., & Dietrich, V. (2002). Geochemical indicators of possible ongoing volcanic unrest at Nisyros Island (Greece). *Geophysical Research Letters*, *29*(16), 6-1–6-4. https://doi.org/10.1029/2001GL014355

Chiodini, G., Caliro, S., Cardellini, C., Granieri, D., Avino, R., Baldini, A., … Minopoli, C. (2010). Long-term variations of the Campi Flegrei, Italy, volcanic system as revealed by the monitoring of hydrothermal activity. *Journal of Geophysical Research*, *115*, B03205. https://doi.org/10.1029/2008JB006258

Chiodini, G., Caliro, S., De Martino, P., Avino, R., & Gherardi, F. (2012). Early signals of new volcanic unrest at Campi Flegrei caldera? Insights from geochemical data and physical simulations. *Geology*, *40*(10), 943–946. https://doi.org/10.1130/G33251.1

Chiodini, G., Cardellini, C., Amato, A., Boschi, E., Caliro, S., Frondini, F., & Ventura, G. (2004). Carbon dioxide earth degassing and seismogenesis in central and southern Italy. *Geophysical Research Letters*, *31*, L07615. https://doi.org/10.1029/2004GL019480

Chiodini, G., Cioni, R., Guidi, M., Raco, B., & Marini, L. (1998). Soil CO_2 flux measurements in volcanic and geothermal areas. *Applied Geochemistry*, *13*(5), 543–552. https://doi.org/10.1016/S0883-2927(97)00076-0

Chiodini, G., Frondini, F., Cardellini, C., Granieri, D., Marini, L., & Ventura, G. (2001). CO_2 degassing and energy release at Solfatara volcano, Campi Flegrei, Italy. *Journal of Geophysical Research*, *106*(B8), 16,213–16,221. https://doi.org/10.1029/2001JB000246

Chiodini, G., Frondini, F., & Raco, B. (1996). Diffuse emission of CO_2 from the Fossa Crater, Vulcano Island (Italy). *Bulletin of Volcanology*, *58*(1), 41–50. https://doi.org/10.1007/s004450050124

Chiodini, G., Granieri, D., Avino, R., Caliro, S., Costa, A., & Werner, C. (2005). Carbon dioxide diffuse degassing and estimation of heat release from volcanic and hydrothermal systems. *Journal of Geophysical Research*, *110*, B08204. https://doi.org/10.1029/2004JB003542

Chiodini, G., Paonita, A., Aiuppa, A., Costa, A., Caliro, S., De Martino, P., … Vandemeulebrouck, J. (2016). Magmas near the critical degassing pressure drive volcanic unrest towards a critical state. *Nature Communications*, *7*, 13,712. https://doi.org/10.1038/ncomms13712

Chiodini, G., Vandemeulebrouck, J., Caliro, S., D'Auria, L., De Martino, P., Mangiacapra, A., & Petrillo, Z. (2015). Evidence of thermal-driven processes triggering the 2005–2014 unrest at Campi Flegrei caldera. *Earth and Planetary Science Letters*, *414*, 58–67. https://doi.org/10.1016/j.epsl.2015.01.012

D'Antonio, M., Civetta, L., Orsi, G., Pappalardo, L., Piochi, M., Carandente, A., … Isaia, R. (1999). The present state of the magmatic system of the Campi Flegrei caldera based on a reconstruction of its behavior in the past 12 ka. *Journal of Volcanology and Geothermal Research*, *91*(2–4), 247–268. https://doi.org/10.1016/S0377-0273(99)00038-4

De Landro, G., Serlenga, V., Russo, G., Amoroso, O., Festa, G., Bruno, P. P., … Zollo, A. (2017). 3D ultra-high resolution seismic imaging of shallow Solfatara crater in Campi Flegrei (Italy): New insights on deep hydrothermal fluid circulation processes. *Scientific Reports*, *7*(1), 3,412. https://doi.org/10.1038/s41598-017-03604-0

De Vivo, B., Rolandi, G., Gans, P. B., Calvert, A., Bohrson, W. A., Spera, F. J., & Belkin, H. E. (2001). New constraints on the pyroclastic eruptive history of the Campanian volcanic Plain (Italy). *Mineralogy and Petrology*, *73*(1–3), 47–65. https://doi.org/10.1007/s007100170010

Del Gaudio, C., Aquino, I., Ricciardi, G. P., Ricco, C., & Scandone, R. (2010). Unrest episodes at Campi Flegrei: A reconstruction of vertical ground movements during 1905–2009. *Journal of Volcanology and Geothermal Research*, *195*(1), 48–56. https://doi.org/10.1016/j.jvolgeores.2010.05.014

Doetsch, J., Linde, N., Pessognelli, M., Green, A. G., & Günther, T. (2012). Constraining 3-D electrical resistance tomography with GPR reflection data for improved aquifer characterization. *Journal of Applied Geophysics*, *78*, 68–76. https://doi.org/10.1016/j.jappgeo.2011.04.008

Ducci, D., & Tranfaglia, G. (2005). L'impatto dei cambiamenti climatici sulle risorse idriche sotterranee in Campania. *Geologi*, *1–4*, 13–21.

Dvorak, J. J., & Gasparini, P. (1991). History of earthquakes and vertical ground movement in Campi Flegrei caldera, southern Italy: Comparison of precursory events to the A.D. 1538 eruption of Monte Nuovo and of activity since 1968. *Journal of Volcanology and Geothermal Research*, *48*(1–2), 77–92. https://doi.org/10.1016/0377-0273(91)90034-W

Finizola, A., Aubert, M., Revil, A., Schütze, C., & Sortino, F. (2009). Importance of structural history in the summit area of Stromboli during the 2002–2003 eruptive crisis inferred from temperature, soil CO_2, self-potential, and electrical resistivity tomography. *Journal of Volcanology and Geothermal Research*, *183*(3–4), 213–227. https://doi.org/10.1016/j.jvolgeores.2009.04.002

Finizola, A., Lénat, J.-F., Macedo, O., Ramos, D., Thouret, J.-C., & Sortino, F. (2004). Fluid circulation and structural discontinuities inside Misti volcano (Peru) inferred from self-potential measurements. *Journal of Volcanology and Geothermal Research*, *135*(4), 343–360. https://doi.org/10.1016/j.jvolgeores.2004.03.009

Finizola, A., Sortino, F., Lénat, J.-F., Aubert, M., Ripepe, M., & Valenza, M. (2003). The summit hydrothermal system of Stromboli. New insights from self-potential, temperature, CO_2 and fumarolic fluid measurements, with structural and monitoring implications. *Bulletin of Volcanology*, *65*(7), 486–504. https://doi.org/10.1007/s00445-003-0276-z

Fournier, R. O. (2006). Hydrothermal systems and volcano geochemistry. In D. Dzurisin (Ed.), *Volcano deformation: Geodetic monitoring techniques* (pp. 323–341). Berlin, Heidelberg: Springer.

Geshi, N., Németh, K., & Oikawa, T. (2011). Growth of phreatomagmatic explosion craters: A model inferred from Suoana crater in Miyakejima volcano, Japan. *Journal of Volcanology and Geothermal Research*, *201*(1–4), 30–38. https://doi.org/10.1016/j.jvolgeores.2010.11.012

Giberti, G., Yven, B., Zamora, M., & Vanorio, T. (2006). Database on laboratory measured data on physical properties of rocks of Campi Flegrei volcanic area (Italy). In A. Zollo, P. Capuano, & M. Corciulo (Eds.), *Geophysical exploration of the Campi Flegrei (Southern Italy) Caldera's interiors: Data, methods and results* (Chap. 4, pp. 179–192). GNV, Naples.

Gottsmann, J., Carniel, R., Coppo, N., Wooller, L., Hautmann, S., & Rymer, H. (2007). Oscillations in hydrothermal systems as a source of periodic unrest at caldera volcanoes: Multiparameter insights from Nisyros, Greece. *Geophysical Research Letters*, *34*, L07307. https://doi.org/10.1029/2007GL029594

Guidoboni, E., & Ciuccarelli, C. (2011). The Campi Flegrei caldera: Historical revision and new data on seismic crises, bradyseisms, the Monte Nuovo eruption and ensuing earthquakes (twelfth century 1582 AD). *Bulletin of Volcanology*, *73*(6), 655–677. https://doi.org/10.1007/s00445-010-0430-3

Hase, H., Hashimoto, T., Sakanaka, S. Y., Kanda, W., & Tanaka, Y. (2005). Hydrothermal system beneath Aso volcano as inferred from self-potential mapping and resistivity structure. *Journal of Volcanology and Geothermal Research*, *143*(4), 259–277. https://doi.org/10.1016/j.jvolgeores.2004.12.005

Hendershot, W. H., Lalande, H., & Duquette, M. (2008). Soil reaction and exchangeable acidity. In M. R. Carter & E. G. Gregorich (Eds.), *Soil sampling and methods of analysis* (2nd ed., pp. 173–178). Boca Raton, FL.

Hochstein, M. P., & Sudarman, S. (1993). Geothermal resources of Sumatra. *Geothermics*, *22*(3), 181–200. https://doi.org/10.1016/0375-6505(93)90042-L

Ingebritsen, S. E., & Sorey, M. L. (1988). Vapor-dominated zones within hydrothermal systems: Evolution and natural state. *Journal of Geophysical Research*, *93*(B11), 13,635–13,655. https://doi.org/10.1029/JB093iB11p13635

Isaia, R., Marianelli, P., & Sbrana, A. (2009). Caldera unrest prior to intense volcanism in Campi Flegrei (Italy) at 4.0 ka B.P.: Implications for caldera dynamics and future eruptive scenarios. *Geophysical Research Letters*, *36*, L21303. https://doi.org/10.1029/2009GL040513

Isaia, R., Vitale, S., Di Giuseppe, M. G., Iannuzzi, E., D'Assisi Tramparulo, F., & Troiano, A. (2015). Stratigraphy, structure, and volcano-tectonic evolution of Solfatara maar-diatreme (Campi Flegrei, Italy). *Geological Society of America Bulletin*, *127*(9–10), 1485–1504. https://doi.org/10.1130/B31183.1

Ishido, T. (2004). Electrokinetic mechanism for the "W"-shaped self-potential profile on volcanoes. *Geophysical Research Letters*, *31*, L15616. https://doi.org/10.1029/2004GL020409

Johnson, T., Versteeg, R., Rockhold, M., Slater, L., Ntarlagiannis, D., Greenwood, W., & Zachara, J. (2012). Characterization of a contaminated wellfield using 3D electrical resistivity tomography implemented with geostatistical, discontinuous boundary, and known conductivity constraints. *Geophysics*, *77*(6), EN85–EN96. https://doi.org/10.1190/geo2012-0121.1

Johnson, T. C., Versteeg, R. J., Ward, A., Day-Lewis, F. D., & Revil, A. (2010). Improved hydrogeophysical characterization and monitoring through parallel modeling and inversion of time-domain resistivity and induced-polarization. *Geophysics*, *75*(4), WA27–WA41. https://doi.org/10.1190/1.347551

Jolly, A. D., Jousset, P., Lyons, J. J., Carniel, R., Fournier, N., Fry, B., & Miller, C. (2014). Seismo-acoustic evidence for an avalanche driven phreatic eruption through a beheaded hydrothermal system: An example from the 2012 Tongariro eruption. *Journal of Volcanology and Geothermal Research*, *286*, 331–347. https://doi.org/10.1016/j.jvolgeores.2014.04.007

Keller, J. (1980). The island of Vulcano. *Rendiconti della Societa Italiana di Mineralogia e Petrologia*, *36*, 369–414.

LaBrecque, D., & Yang, X. (2001). Difference inversion of ERT data: A fast inversion method for 3-D in situ monitoring. *Journal of Environmental and Engineering Geophysics*, *6*(2), 83–89. https://doi.org/10.4133/JEEG6.2.83

Loke, M. H. (2003). Rapid 2D resistivity and IP inversion using the least-squares method: Geolectrical imaging 2-D and 3-D—Geotomo software (pp. 125). Retrieved from http://www.geolectrical.com, accessed August 10, 2003.

Loke, M. H., & Barker, R. D. (1996). Rapid least-squares inversion of apparent resistivity pseudosections by a quasi-Newton method[1]. *Geophysical Prospecting*, *44*(1), 131–152. https://doi.org/10.1111/j.1365-2478.1996.tb00142.x

Mayer, K., Scheu, B., Montanaro, C., Yilmaz, T. I., Isaia, R., Aßbichler, D., & Dingwell, D. B. (2016). Hydrothermal alteration of surficial rocks at Solfatara (Campi Flegrei): Petrophysical properties and implications for phreatic eruption processes. *Journal of Volcanology and Geothermal Research*, *320*, 128–143. https://doi.org/10.1016/j.jvolgeores.2016.04.020

McNeill, J. D. (1980). Electromagnetic terrain conductivity measurement at low induction numbers, Geonics Ltd**,** Technical Note TN-6.

Milsch, H., Kristinsdóttir, L. H., Spangenberg, E., Bruhn, D., & Flóvenz, Ó. G. (2010). Effect of the water–steam phase transition on the electrical conductivity of porous rocks. *Geothermics*, *39*(1), 106–114. https://doi.org/10.1016/j.geothermics.2009.09.001

Neri, A., Bevilacqua, A., Esposti Ongaro, T., Isaia, R., Aspinall, W. P., Bisson, M., … Vitale, S. (2015). Quantifying volcanic hazard at Campi Flegrei caldera (Italy) with uncertainty assessment: 2. Pyroclastic density current invasion maps. *Journal of Geophysical Research: Solid Earth*, *120*, 2330–2349. https://doi.org/10.1002/2014JB011776

Orsi, G., Di Vito, M., & Isaia, R. (2004). Volcanic hazard assessment at the restless Campi Flegrei caldera. *Bulletin of Volcanology*, *66*(6), 514–530. https://doi.org/10.1007/s00445-003-0336-4

Petrosino, S., Damiano, N., Cusano, P., Di Vito, M. A., de Vita, S., & Del Pezzo, E. (2012). Subsurface structure of the Solfatara volcano (Campi Flegrei caldera, Italy) as deduced from joint seismic-noise array, volcanological and morphostructural analysis. *Geochemistry, Geophysics, Geosystems*, *13*, Q07006. https://doi.org/10.1029/2011GC004030

Pilz, M., Parolai, S., & Woith, H. (2017). A 3-D algorithm based on the combined inversion of Rayleigh and Love waves for imaging and monitoring of shallow structures. *Geophysical Journal International*, *209*(1), ggx005–ggx166. https://doi.org/10.1093/gji/ggx005

Rabaute, A., Yven, B., Chelini, W., & Zamora, M. (2003). Subsurface geophysics of the Phlegrean fields: New insights from downhole measurements. *Journal of Geophysical Research*, *108*, 2171. https://doi.org/10.1029/2001JB001436

Revil, A., Finizola, A., Piscitelli, S., Rizzo, E., Ricci, T., Crespy, A., … Suski, B. (2008). Inner structure of La Fossa di Vulcano (Vulcano Island, southern Tyrrhenian Sea, Italy) revealed by high-resolution electric resistivity tomography coupled with self-potential, temperature, and CO_2 diffuse degassing measurements. *Journal of Geophysical Research*, *113*, B07207. https://doi.org/10.1029/2007JB005394

Revil, A., Finizola, A., Ricci, T., Delcher, E., Peltier, A., Barde-Cabusson, S., … Tsang Hin Sun, E. (2011). Hydrogeology of Stromboli Volcano, Aeolian Islands (Italy) from the interpretation of resistivity tomograms, self-potential, soil temperature and soil CO_2 concentration measurements. *Geophysical Journal International*, *186*(3), 1078–1094. https://doi.org/10.1111/j.1365-246X.2011.05112.x

Revil, A., Finizola, A., Sortino, F., & Ripepe, M. (2004). Geophysical investigations at Stromboli Volcano, Italy: Implications for ground water flow and paroxysmal activity. *Geophysical Journal International*, *157*(1), 426–440. https://doi.org/10.1111/j.1365-246X.2004.02181.x

Revil, A., Hermitte, D., Spangenberg, E., & Cochemé, J. J. (2002). Electrical properties of zeolitized volcaniclastic materials. *Journal of Geophysical Research*. *107*, 2168. https://doi.org/10.1029/2001JB000599

Revil, A., & Jardani, A. (2013). *The self-potential method: Theory and applications in environmental geosciences*. New York: Cambridge University Press. https://doi.org/10.1017/CBO9781139094252

Revil, A., Johnson, T. C., & Finizola, A. (2010). Three-dimensional resistivity tomography of Vulcan's forge, Vulcano Island, southern Italy. *Geophysical Research Letters*, *37*, L15308. https://doi.org/10.1029/2010GL043983

Revil, A., Le Breton, M., Niu, Q., Wallin, E., Haskins, E., & Thomas, D. M. (2017a). Induced polarization of volcanic rocks. 2. Influence of pore size and permeability. *Geophysical Journal International*, *208*(2), 814–825. https://doi.org/10.1093/gji/ggw382

Revil, A., Le Breton, M., Niu, Q., Wallin, E., Haskins, E., & Thomas, D. M. (2017b). Induced polarization of volcanic rocks – 1. Surface versus quadrature conductivity. *Geophysical Journal International*, *208*(2), 826–844. https://doi.org/10.1093/gji/ggw444

Revil, A., Murugesu, M., Prasad, M., & Le Breton, M. (2017). Alteration of volcanic rocks: A new non-intrusive indicator based on induced polarization measurements. *Journal of Volcanology and Geothermal Research*, *341*, 351–362. https://doi.org/10.1016/j.jvolgeores.2017.06.016

Revil, A., & Pezard, P. A. (1998). Streaming electrical potential anomaly along faults in geothermal areas. *Geophysical Research Letters*, *25*(16), 3197–3200. https://doi.org/10.1029/98GL02384

Roberts, J. J., Duba, A. G., Bonner, B. P., & Kasameyer, P. W. (2001). The effects of capillarity on electrical resistivity during boiling in metashale from scientific corehole SB-15-D, The Geysers, California, USA. *Geothermics*, *30*(2–3), 235–254. https://doi.org/10.1016/S0375-6505(00)00052-3

Rosas-Carbajal, M., Komorowski, J.-C., Nicollin, F., & Gibert, D. (2016). Volcano electrical tomography unveils edifice collapse hazard linked to hydrothermal system structure and dynamics. *Scientific Reports*, *6*(1), 29,899. https://doi.org/10.1038/srep29899

Rosi, M., Sbrana, A., & Principe, C. (1983). The phlegraean fields: Structural evolution, volcanic history and eruptive mechanisms. *Journal of Volcanology and Geothermal Research*, *17*(1–4), 273–288. https://doi.org/10.1016/0377-0273(83)90072-0

Serra, M., Festa, G., Roux, P., Gresse, M., Vandemeulebrouck, J., & Zollo, A. (2016). A strongly heterogeneous hydrothermal area imaged by surface waves: The case of Solfatara, Campi Flegrei, Italy. *Geophysical Journal International*, *205*(3), 1813–1822. https://doi.org/10.1093/gji/ggw119

Si, H. (2015). TetGen, a Delaunay-based quality tetrahedral mesh generator. *ACM Transactions on Mathematical Software*, *41*(2), 1–36. https://doi.org/10.1145/2629697

Smith, V. C., Isaia, R., & Pearce, N. J. G. (2011). Tephrostratigraphy and glass compositions of post-15 kyr Campi Flegrei eruptions: Implications for eruption history and chronostratigraphic markers. *Quaternary Science Reviews*, *30*(25–26), 3638–3660. https://doi.org/10.1016/j.quascirev.2011.07.012

Tassi, F., Vaselli, O., Papazachos, C. B., Giannini, L., Chiodini, G., Vougioukalakis, G. E., … Panagiotopoulos, D. (2013). Geochemical and isotopic changes in the fumarolic and submerged gas discharges during the 2011–2012 unrest at Santorini caldera (Greece). *Bulletin of Volcanology*, *75*(4), 711. https://doi.org/10.1007/s00445-013-0711-8

Thien, B. M. J., Kosakowski, G., & Kulik, D. A. (2015). Differential alteration of basaltic lava flows and hyaloclastites in Icelandic hydrothermal systems. *Geothermal Energy*, *3*(1), 11. https://doi.org/10.1186/s40517-015-0031-7

Troiano, A., Giuseppe, M. G. D., Patella, D., Troise, C., & Natale, G. D. (2014). Electromagnetic outline of the Solfatara–Pisciarelli hydrothermal system, Campi Flegrei (southern Italy). *Journal of Volcanology and Geothermal Research*, *277*, 9–21. https://doi.org/10.1016/j.jvolgeores.2014.03.005

Ussher, G., Harvey, C., Johnstone, R., & Anderson, E. (2000). Understanding the resistivities observed in geothermal systems. In *World geothermal congress proceedings* (pp. 1915–1920). Japan: Kyusyu-Tohoku.

Vanorio, T., Prasad, M., Patella, D., & Nur, A. (2002). Ultrasonic velocity measurements in volcanic rocks: Correlation with microtexture. *Geophysical Journal International*, *149*(1), 22–36. https://doi.org/10.1046/j.0956-540x.2001.01580.x

Villasante-Marcos, V., Finizola, A., Abella, R., Barde-Cabusson, S., Blanco, M. J., Brenes, B., … Trigo, P. (2014). Hydrothermal system of Central Tenerife volcanic complex, Canary Islands (Spain), inferred from self-potential measurements. *Journal of Volcanology and Geothermal Research*, *272*, 59–77. https://doi.org/10.1016/j.jvolgeores.2013.12.007

Vito, M. A. D., Isaia, R., Orsi, G., Southon, J., de Vita, S., D'Antonio, M., … Piochi, M. (1999). Volcanism and deformation since 12,000 years at the Campi Flegrei caldera (Italy). *Journal of Volcanology and Geothermal Research*, *91*(2–4), 221–246. https://doi.org/10.1016/S0377-0273(99)00037-2

Waxman, M. H., & Smits, L. J. M. (1968). Electrical conductivities in oil-bearing shaly sands. *Society of Petroleum Engineers Journal*, *8*(02), 107–122. https://doi.org/10.2118/1863-A

Werner, C., Evans, W. C., Kelly, P. J., McGimsey, R., Pfeffer, M., Doukas, M., & Neal, C. (2012). Deep magmatic degassing versus scrubbing: Elevated CO_2 emissions and C/S in the lead-up to the 2009 eruption of Redoubt Volcano, Alaska. *Geochemistry, Geophysics, Geosystems*, *13*, Q03015. https://doi.org/10.1029/2011GC003794

White, D. E., Muffler, L. J. P., & Truesdell, A. H. (1971). Vapor-dominated hydrothermal systems compared with hot-water systems. *Economic Geology*, *66*(1), 75–97. https://doi.org/10.2113/gsecongeo.66.1.75

Zhou, J., Revil, A., Karaoulis, M., Hale, D., Doetsch, J., & Cuttler, S. (2014). Image-guided inversion of electrical resistivity data. *Geophysical Journal International*, *197*(1), 292–309. https://doi.org/10.1093/gji/ggu001

Zimbelman, D. R., Rye, R. O., & Breit, G. N. (2005). Origin of secondary sulfate minerals on active andesitic stratovolcanoes. *Chemical Geology*, *215*(1–4), 37–60. https://doi.org/10.1016/j.chemgeo.2004.06.056

Zollo, A., Maercklin, N., Vassallo, M., Dello Iacono, D., Virieux, J., & Gasparini, P. (2008). Seismic reflections reveal a massive melt layer feeding Campi Flegrei caldera. *Geophysical Research Letters*, *35*, L12306. https://doi.org/10.1029/2008GL034242